Doppler-Free Saturated Fluorescence Spectroscopy of Lithium Using a Stabilized Frequency Comb

by

Michael E. Rowan

Oberlin College
Department of Physics
April 2013

Summary

The lineshapes of the D1 ($2^2S_{1/2} \rightarrow 2^2P_{1/2}$) and D2 ($2^2S_{3/2} \rightarrow 2^2P_{1/2}$) transitions in lithium were measured using a diode laser that was frequency-stabilized to a Ti:Sapphire 1 GHz optical frequency comb. The excitation was achieved by retroreflecting the diode laser, in effect producing Doppler-free profiles for the center frequencies of transitions. The observed spectra were compared to density matrix calculations to gain insight into systematic effects including the dependence of Doppler-free profiles on power and polarization angle of the diode. For certain transitions, the method of saturated fluorescence spectroscopy inevitably leads to the presence of extra resonances known as crossover signals. Our preliminary data suggest that the presence of this complicating effect may render saturated fluorescence spectroscopy an ineffective technique for resolution of transitions whose relative separation is on the order of the natural linewidth of Li.

Contents

List of Figures

Acknowledgments

My deep gratitude to my adviser, Jason Stalnaker, is beyond description. Without his encouragement, patience, optimism, and support, this work would not have been completed. I am incredibly grateful that I have had the opportunity to learn from him. He has been outstanding in every way, and I could not have imagined having a better adviser and mentor.

I also owe sincere thanks to those who worked on this project or related projects before me. It is a great pleasure to thank Jacob Baron, Sophia Chen, Sean Bernfeld, and José Almaguer. Indeed, this work is cumulative in nature, and without their contributions it would not have been possible. Additionally, their theses were invaluable resources while working on my own. I would also like to thank Jacob and Sophia for their company in the lab.

Next, I would like to thank my friends and fellow physics students at Oberlin, including those currently at Oberlin and those who have graduated. They have offered wonderful companionship and have contributed to my education and general quality of life, whether working on physics problem sets, eating meals together, or simply being in the same classes. Additionally, I am immensely thankful for the humor they have injected into my life. I offer my sincere thanks to (in alphabetical order) Anthony Ruda, Conrad Luecke, Chetan Poudel, Dagmawi Gebreselasse, David Morris, Derek Lange, Edward Russell, Greg Stevens, Harry Rubin-Falcone, Jocienne Nelson, Joe Beck, Kathryn Hasz, Kenny Yi, Kirsten Liebl, Lesley Whitaker, Maayan Dagan, Mikaela Larkin, Nic Zhang, Noah Jones, Sam Berney, and Zachary Mark.

Lastly, I would like to thank my family, especially my parents, my brother, my Grandma, and my Aunt Mare. Their support is and has been deeply appreciated.

Chapter 1

Introduction to the Experiment

1.1 Motivation

For many years, atomic spectroscopy experiment has provided insight into fundamental physics. The field has led to a number of important discoveries, including fine and hyperfine structure of atoms, the Stark effect, Zeeman splitting, and other developments in the understanding of atomic structure. As precision measurement techniques and atomic structure calculations continue to improve, the alkali metals have emerged as promising candidates for comparison of atomic theory and experiment. With recent improvements in three-electron atomic structure calculations, lithium (Li), in particular, has become the focus of many research efforts. A number of calculations have yielded highly accurate predictions for Li atomic structure [1–7]. However, there are considerable discrepancies in experimental tests of the calculations (see Fig. 1.1). Precision measurement of Li has not yet reached an accuracy matching that of the structure calculations.

Further study of Li will provide high-precision tests of quantum electrodynamics (QED), effects of which are incorporated into atomic structure calculations. At the present levels of accuracy, QED plays an important role in predictions related to fine and hyperfine

structure. The small uncertainties of these calculations provides motivation for precision atomic spectroscopy experiments to achieve measurements with similar levels of accuracy.

A number of previous atomic structure measurements of Li are in disagreement. In particular, there is a significant discrepancy in measurements of the isotope shifts of the D1 ($2^2S_{1/2} \rightarrow 2^2P_{1/2}$) and D2 ($2^2S_{3/2} \rightarrow 2^2P_{1/2}$) transitions of Li (see Fig. 1.1). In addition, these measurements concede the presence of systematic effects. Similarly, measurements of the fine structure splitting of the $2P$ state in ^{6,7}Li are in serious disagreement. Discrepancy among measurements of the D2 lines may have been resolved by Sansonetti et. al. [8], who found that the D2 lineshapes varied dramatically depending on the polarization of the laser, a result of quantum interference. However, this effect does not explain disagreement in measurements of the D1 transitions.

Further experiments are needed to resolve the conflict surrounding prior measurements of Li atomic structure. In this experiment, we aim to eventually reach levels of accuracy of less than 5 kHz. This uncertainty would be less than those of recent atomic structure calculations [14], [15], and [16].

1.2 Summary

In this experiment, we study the atomic structure of Li using methods of high-precision atomic spectroscopy. More specifically, we use a method called saturated fluorescence spectroscopy to achieve Doppler-free resolution of the atomic lineshape. This involves retroreflecting a laser beam across a beam of atomic Li. The systematic uncertainty in this experiment is minimized by frequency-stabilizing the pump laser. To do this, we lock the frequency of the diode laser to a mode of a stabilized frequency comb. The frequency comb is a set of equally spaced colors in frequency space. The the offset frequency, the spacing

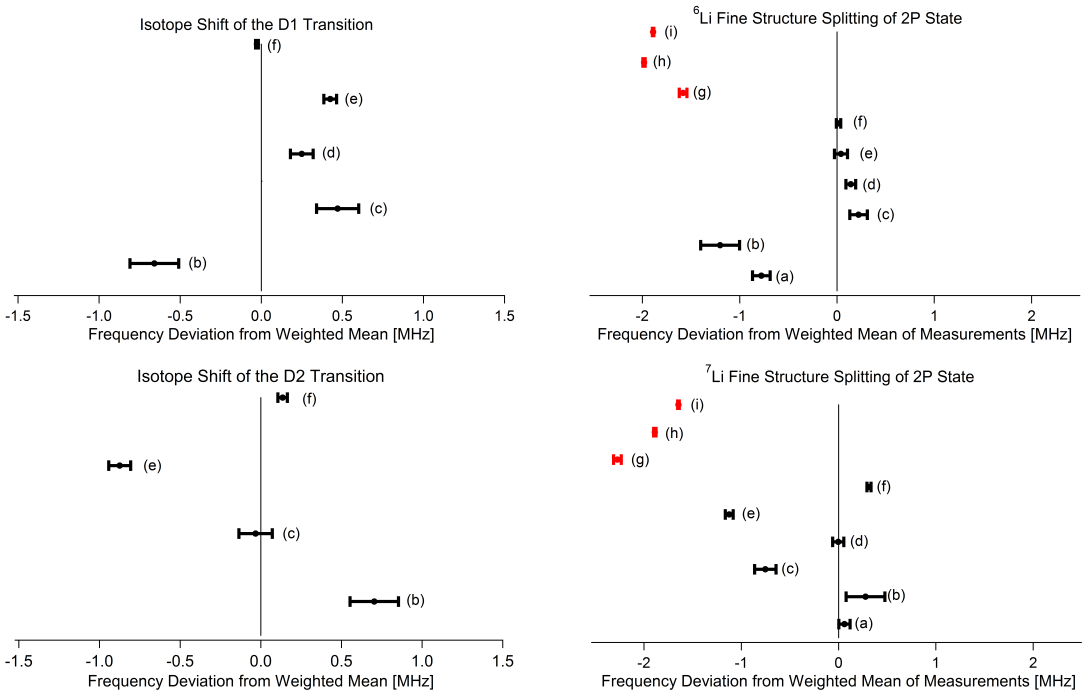

Figure 1.1: Previous measurements and calculation of Li isotope shifts and fine structure splitting for the D1 and D2 transitions. Red points are theory calculations, black points are experimental measurements. The disagreement provides motivation for further study of lithium. Also, the error bars on the theory points are very small, so the experiments should be able to match these error bars, at the least. The isotope shifts suffer from systematic error. Points labeled with (a), (b), (c), (d), (e), (f), (g), (h), and (i) comes from Refs. [9], [10], [11], [12], [13], [8], [14], [15], and [16], respectively.

between modes, and the number of modes are known, then any particular mode of the comb can be determined. Since the mode of the frequency comb can be determined and controlled, the frequency of the stabilized pump laser can also be known to a high level of precision. We also aim to eventually give careful consideration to systematic effects including ac Stark shifts, Zeeman splitting, and polarization angle of the pump laser.

Chapter 2

Theory

2.1 Atomic Energy Levels

In quantum mechanics, the Schrödinger equation is used to describe the evolution of a particle's wave function. By solving the time-independent version, we can obtain the energy eigenvalues that represent the energies of the stationary states. For example, we can solve for the allowed energies of the hydrogen atom by solving the time-independent Schrödinger equation. Though hydrogen is the only atom that admits an exact solution, it is similar to other simple atoms, such as lithium. As a result, the hydrogen solution serves as the basis for calculations involving more complicated atoms. In this section, the Schrödinger equation is introduced so that it can later be used to solve for the allowed energy levels of the hydrogen atom. Reference [17] is followed.

For a particle moving in a potential $V(r,t)$, the Schrödinger Eqn. reads

$$i\hbar\frac{\partial}{\partial t}\Psi(r,t) = \left(-\frac{\hbar^2}{2m}\nabla^2 + V(r,t)\right)\Psi(r,t). \tag{2.1}$$

When the potential is independent of the time coordinate, the Schrödinger equation allows

the solutions

$$\Psi(r,t) = \psi(r)e^{-\frac{i}{\hbar}Et}, \tag{2.2}$$

where E is a real number and $\psi(r)$ satisfies the eigenvalue equation

$$H\psi = E\psi. \tag{2.3}$$

When a system's energy is measured, the result must be one of the eigenvalues E of the Hamiltonian operator.

2.2 Spectroscopic Notation

When referring to a particular energy state for an atom, the standard notation is

$$^{2S+1}L_J, \tag{2.4}$$

where S is total spin angular momentum, L is the total orbital angular momentum, and $J = L + S$ is is total electronic angular momentum. To determine the allowed values for J, the numbers S and L are added as vectors so that the allowed values of J are

$$|L - S| < J < L + S. \tag{2.5}$$

Traditionally, capitalized quantum numbers are used when referring to *totals* (total orbital angular momentum, total spin angular momentum, etc.) and are therefore appropriate for multi-electron atoms. Lowercase quantum numbers refer to single-electron atoms, for example, hydrogen.

2.3 Gross Structure

One of the fundamental features of quantum mechanics is quantization of energy. This stands in stark contrast to ordinary experience, in which objects are allowed to assume

energies from a continuous range of values. Nevertheless, the atomic scale is small enough that quantum effects are significant, and indeed, atomic energy levels are quantized. The goal of this section is to derive the allowed energy levels for a single electron atom, hydrogen. This solution often serves as a basis for atomic spectra calculations. Here, we present the derivation given in Ref. [17].

A hydrogen atom consists of a proton of charge $+e$ and an electron of charge $-e$. The proton and electron interact by means of a central potential given by

$$V(r) = -\frac{e^2}{4\pi\epsilon_0 r}. \tag{2.6}$$

The total energy of our atom can be separated into two parts, one corresponding to the motion of the center of mass, the other corresponding to the energy of the relative motion. The Hamiltonian for the motion of relative energy is

$$H = \frac{p^2}{2\mu} - \frac{e^2}{4\pi\epsilon_0 r}, \tag{2.7}$$

where p is the relative momentum and μ is the reduced mass. If we work in the center of mass frame, then the energy of the center of mass is zero, and Schrödinger's equation yields

$$\left(-\frac{\hbar^2}{2\mu}\nabla^2 - \frac{e^2}{4\pi\epsilon_0 r}\right)\Psi(r) = E\Psi(r). \tag{2.8}$$

This equation can be separated using spherical coordinates. That is, a particular solution to the wave equation can be rewritten in the form

$$\Psi(r,\theta,\phi) = R_l(r)Y_{l,m}(\theta,\phi), \tag{2.9}$$

where $R_l(r)$ is the radial part and $Y_{l,m}$ is a spherical harmonic. The radial part satisfies the equation

$$\left\{\frac{-\hbar^2}{2\mu}\left(\frac{1}{r^2}\frac{d}{dr}\left(r^2\frac{d}{dr}\right) - \frac{l(l+1)}{r^2}\right)\frac{e^2}{(4\pi\varepsilon_0)r}\right\}R_l(r) = ER_l(r). \tag{2.10}$$

This equation is simplified by the introduction of the function

$$u_l(r) = rR_l(r). \tag{2.11}$$

Using this new function and Eq. 2.10, it can be shown that

$$\frac{d^2u_l}{dr^2} + \frac{2\mu}{\hbar^2}(E - V_{eff}(r))u_l(r) = 0 \tag{2.12}$$

where we have introduced an effective potential

$$V_{eff} = -\frac{e^2}{4\pi\epsilon_0 r} + \frac{l(l+1)\hbar^2}{2\mu r^2}. \tag{2.13}$$

To solve Eq. 2.12, we will look for solutions satisfying the boundary condition

$$u_l(0) = 0, \tag{2.14}$$

so that the wave function $\Psi(r)$ does not blow up at the origin. Equation 2.12 can be simplified through the introduction of the quantities

$$\rho = \sqrt{\frac{-8\mu E}{\hbar^2}}r \tag{2.15}$$

and

$$\lambda = \alpha\sqrt{\frac{-\mu c^2}{2E}}, \tag{2.16}$$

where $\alpha = \frac{e^2}{4\pi\epsilon_0\hbar c}$ is the fine structure constant. Equation 2.12 then reduces to

$$\left(\frac{d^2}{d\rho^2} - \frac{l(l+1)}{\rho^2} + \frac{\lambda}{\rho} - \frac{1}{4}\right)u_l(\rho) = 0. \tag{2.17}$$

By searching for solutions of the form

$$u_l(\rho) = \mathrm{e}^{\frac{-\rho}{2}}\rho^{l+1}\sum_{k=0}^{\infty} c_k\rho^k, \qquad c_0 \neq 0, \tag{2.18}$$

it can be shown that the eigenvalues of Eq. 2.17 are integers

$$\lambda = n, \qquad n = 1, 2, \ldots \tag{2.19}$$

Substituting $\lambda = n$ into Eq. 2.15, solving for E, we obtain the allowed energy levels of the hydrogen atom,

$$E_n = \frac{e^2}{4\pi\epsilon_0 a_0}\frac{1}{n^2}, \qquad n = 1, 2, 3, \ldots, \tag{2.20}$$

where we have assumed the mass of the proton is much greater than the mass of the electron and set $\mu = m_e$ and have used $a_0 = \frac{4\pi\epsilon_0\hbar^2}{m_e e^2}$, the Bohr radius.

2.3.1 Isotope Shifts

The energy levels of an atom are also shifted, but not split, depending on the isotope. The shift is caused by the finite mass of the nucleus and the nuclear charge distribution within a finite volume. For single-electron atoms, it can be seen from Eq. 2.23 that if the atom is not assumed to be of infinite mass, then the mass of the electron is replaced by the reduced mass $\mu = \frac{m_e m_p}{m_e + m_p}$, and the energy levels are shifted accordingly. For multi-electron atoms, an effect known as "mass polarization" further shifts the energy levels [17].

Since different atoms have different nuclear charge configurations, the electric potential does not obey the $\frac{1}{r}$ law inside the nucleus, rather it depends on the particular charge configuration. An estimate of this effect can be obtained by assuming that the charge distributes uniformly throughout a sphere of radius $R = r_0 a^{1/3}$. With this assumption, the electric potential due to the nucleus is found to obey the $1/r$ law outside the sphere of radius R and is found to differ inside the sphere [17]:

$$V(r) = \begin{cases} \frac{Ze^2}{4\pi\varepsilon_0 2R}\left(\frac{r^2}{R^2} - 3\right) & r \leq R \\ -\frac{Ze^2}{4\pi\varepsilon_0 r} & r \geq R. \end{cases} \tag{2.21}$$

Applying first order perturbation theory, the energy difference between two isotopes due to

nuclear charge distribution is found to be [17]

$$\delta E \approx \frac{Z^5 e^2}{4\pi\varepsilon_0}\frac{4}{5}\frac{R^2\delta R}{a_\mu^3 n^3 R}, \tag{2.22}$$

where δR is the difference between the radii of the isotopes and $a_\mu = a_0(m/\mu)$. We can see that the isotope shift δE is larger for atoms with greater Z. Additionally, the energy shift is most significant for energy states with lower n. The isotope with the greater radius assumes the higher energy value.

Lithium has two stable isotopes, ^{7}Li and ^{6}Li, with relative abundances of 92.41% and 7.59% [18]. The D1 and D2 lines of ^{7}Li are shifted up by approximately 10.5 GHz relative to the D1 and D2 lines of ^{6}Li. See Fig. 2.1.

2.3.2 Fine Structure

In section 2.3, the energy levels of hydrogen were shown to be

$$E_n = \frac{e^2}{4\pi\epsilon_0 a_0}\frac{1}{n^2}, \qquad n = 1, 2, 3, \ldots. \tag{2.23}$$

Previously, the Hamiltonian was assumed to include one term for the electron kinetic energy and another for the Coulomb potential. However, additional corrections reveal a more nuanced atomic structure, known as fine structure. Fine structure corrections are the result of two additional effects, one relating to relativistic kinetic energy and another that comes from spin-orbit interaction.

The relativistic correction is derived by substituting relativistic kinetic energy for the classical kinetic energy in the Hamiltonian. Expanding the formula for relativistic kinetic energy in a Taylor series, we obtain

$$T = \frac{mc^2}{\sqrt{1-\frac{v}{c}^2}} - mc^2 = \frac{p^2}{2m} - \frac{p^4}{8m^3c^2} + \ldots, \tag{2.24}$$

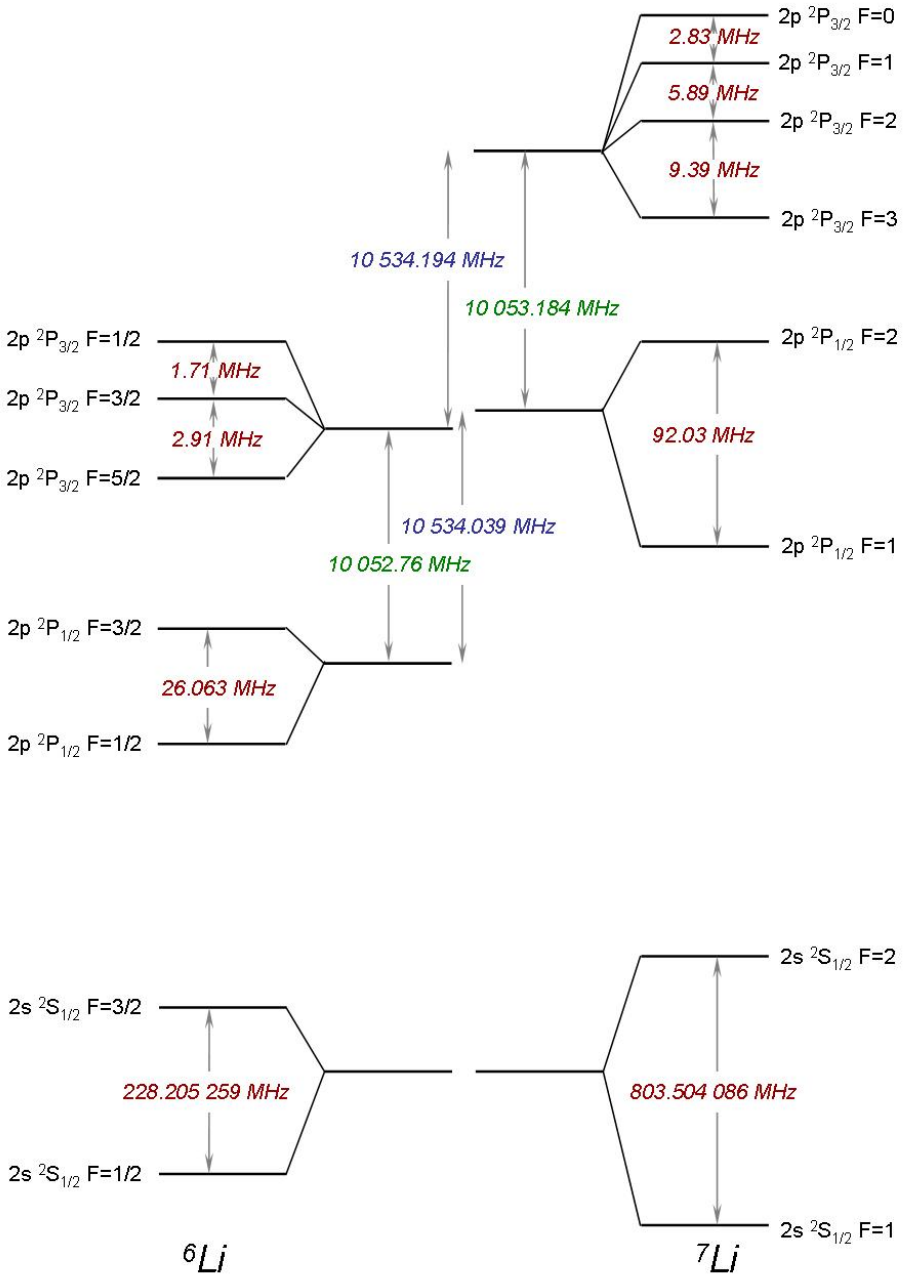

Figure 2.1: The hyperfine splitting in the D2 line of ^{6}Li D2 transition is on the order of 6 MHz, which is about the natural linewidth of the transition.

so that the first-order relativistic correction is

$$H'_{rel} = -\frac{\hat{p}^4}{8m^3c^2}. \tag{2.25}$$

The correction to the energy levels is computed by treating the correction as a perturbation and calculating the expectation value of H'_{rel}. The result is [19]

$$E^{(1)}_{rel} = -\frac{E_n^2}{2mc^2}\Big[\frac{4n}{l+\frac{1}{2}} - 3\Big]. \tag{2.26}$$

In general, this correction is on the order of $E_1/(m_e c^2) \approx 10^{-3}$ eV. We note that the relativistic correction results in just a negative shift to the hydrogen energy levels. The correction will be largest for states with small n and l.

The spin-orbit correction comes about when one considers the orbiting electron's frame of reference. In the electron's frame, the proton is in orbit, which produces a magnetic field. This results in different energies depending on the alignment of the electron's magnetic moment $\vec{\mu}$ with the direction of the magnetic field $\vec{B}$. The Hamiltonian equation for an electron in a magnetic field is

$$H'_{so} = -\vec{\mu} \cdot \vec{B}. \tag{2.27}$$

To make use of this, we must find the expectation value of $\vec{\mu}$ for a given atomic state.

In the frame of the electron, we can consider the proton, which orbits with period T, to be a loop of current given by

$$I = \frac{e}{T}. \tag{2.28}$$

From the Biot-Savart law, we know that the magnetic field given by a circular current is just

$$B = \frac{\mu_0 I}{2r} = \frac{\mu_0 e}{2rT}. \tag{2.29}$$

However, we also know that in the rest frame of the proton, the electron has an angular momentum $L = mrv = 2\pi r^2 m/T$. Furthermore, $\vec{L}$ and $\vec{B}$ both point in the same direction,

so we have

$$\vec{B} = \frac{\mu_0 e}{4\pi m r^3}\vec{L}. \tag{2.30}$$

where $\vec{L}$ is the total orbital angular momentum. Writing $\vec{B}$ in this form will allow us to express Eq. 2.27 in terms of $\vec{L}$ and $\vec{S}$ if we can write the electron dipole moment μ in terms of the spin. It turns out that [19]

$$\vec{\mu} = -\frac{e}{m}\vec{S}, \tag{2.31}$$

where S is the total spin angular momentum. We can provide some motivation for this by considering the classical picture. Classically, the magnetic dipole moment of a ring is defined as the current (I) times the area ($2\pi r^2$) of the ring:

$$\mu = \frac{e}{T}2\pi r^2. \tag{2.32}$$

If we call the angular momentum of the ring S and recall that a ring has a moment of inertia mr^2, then classically we have

$$S = I\omega = \frac{mr^2 2\pi}{T}. \tag{2.33}$$

Since μ and S will be antiparallel, since the charge e is negative, this classical calculation yields

$$\vec{\mu} = -\frac{e}{2m}\vec{S}. \tag{2.34}$$

This differs from Eq. 2.31 by a factor of 2, which is explained in the relativistic theory of the electron.

Using Eqs. 2.30 and 2.31, we can write Eq. 2.27 as

$$H'_{so} = \Big(\frac{e^2}{4\pi\epsilon_0}\Big)\frac{1}{m^2c^2r^3}\vec{L}\cdot\vec{S}, \tag{2.35}$$

where we have used $c^2 = \frac{1}{\mu_0\epsilon_o}$. Since the electron's reference frame is not actually an inertial reference frame, as the electron accelerates around the proton, Eq. 2.35 requires an

additional correction known as "Thomas precession" [19]. This inserts a factor of $\frac{1}{2}$, so that

$$H'_{so} = \Big(\frac{e^2}{8\pi\epsilon_0}\Big)\frac{1}{m^2c^2r^3}\vec{S}\cdot\vec{L}. \tag{2.36}$$

This simplifies if we define the total angular momentum $\vec{J}$ by $\vec{J} = \vec{L} + \vec{S}$ and consider the identity $\vec{L}\cdot\vec{S} = \frac{1}{2}(J^2 - L^2 - S^2)$, so that the eigenvalues of a state with quantum numbers l, s, j, and m_j are

$$\frac{\hbar^2}{2}[j(j+1) - l(l+1) - s(s+1)]. \tag{2.37}$$

In the case of hydrogen, $s = 1/2$ while the expectation value of $\frac{1}{r^3}$ is [19]

$$\langle\frac{1}{r^3}\rangle = \frac{1}{l(l+1/2)(l+1)n^3a_0^3}. \tag{2.38}$$

In terms of the previously calculated energy levels of hydrogen, it can be shown that the spin-orbit correction is

$$E^{(1)}_{so} = \frac{E_n^2}{mc^2}\left\{\frac{n[j(j+1) - l(l+1) - 3/4]}{l(l+1/2)(l+1)}\right\}. \tag{2.39}$$

The numerator of Eq. 2.39 can change sign depending on the value of j. For example, if we set $j = l \pm 1/2$, then in the case $j = l + 1/2$, Eq. 2.39 reduces to

$$E^{(1)}_{so,j=l+1/2} = \frac{E_n^2}{mc^2}\left\{\frac{n}{(l+1/2)(l+1)}\right\}, \tag{2.40}$$

which is positive. However, if $j = l - 1/2$, the equation reduces to

$$E^{(1)}_{so,j=l-1/2} = \frac{E_n^2}{mc^2}\left\{-\frac{n(l+1)}{l(l+1/2)(l+1)}\right\}, \tag{2.41}$$

which is negative. So, depending on the alignment of the spin and orbital angular momentum, the spin-orbit correction can be be positive or negative. This means that the the energy levels are split rather than just shifted. We can also see that spin-orbit coupling lifts the degeneracy of l and s.

Finally, one can combine the relativistic and spin-orbit corrections to obtain the fine-structure energy levels. To first order,

$$E_{f-s}^{(1)} = \frac{E_n^2}{2mc^2}\Big(3 - \frac{4n}{j+1/2}\Big), \tag{2.42}$$

or in terms of the fine-structure constant α,

$$E_{fs}^{(1)} = -\frac{13.6 \text{ eV}}{n^2}\left(1 + \frac{\alpha^2}{n^2}\left(\frac{n}{j+1/2} - \frac{3}{4}\right)\right). \tag{2.43}$$

It is interesting to note that even though the spin-orbital correction and relativistic corrections arise from entirely different mechanisms, they are both on the order of $\frac{E_n^2}{2mc^2}$.

2.4 Single-Electron vs. Multi-Electron Atoms

Up to now we have focused on the atomic structure of hydrogen, a one-electron atom. There are several important differences between single-electron and multi-electron atoms. One complicating factor in the latter is that electrons in outer orbitals experience shielding from the full charge of the nucleus. As a result, electrons that spend more time near the nucleus will be more tightly bound than those that spend more time further from the nucleus. Due to this shielding effect, the deviation from the hydrogen energy levels is greatest for S terms, smaller for P terms, and even smaller for D terms, etc. [20]. Indeed, the equation for energy levels of a one-electron atom (Eq. 2.23) does not apply to multi-electron atoms.

On the other hand, certain multi-electron atoms are similar to hydrogen, in particular the alkali atoms. These atoms consist of a filled electron shell with one orbiting electron, which is very similar to the structure of hydrogen.

In our experiment, we are examining transitions from the ground state of lithium to the fine-structure doublet of the first excited configuration. In the ground state ($^2S_{1/2}$) of

lithium, $L = 0$. We can see from Eq. 2.39 that with an orbital angular momentum of zero, the spin-orbital correction provides no contribution to the ground state energy. However, in the first excited states, $L = 1$ and $S = 1/2$, so that the $2P$ state is split into two energy levels, namely the $^2P_{1/2}$ and $^2P_{3/2}$ states. The $^2S_{1/2} \rightarrow^2 P_{1/2}$ and $^2S_{1/2} \rightarrow^2 P_{3/2}$ transitions are commonly referred to as the "D1" and "D2" transitions, respectively. The separation between these transitions is about 10 GHz. Figure 2.2 shows an energy level diagram for lithium.

2.5 Hyperfine Structure

If the spectral structure of an atom is probed to a very high level of precision, another level of splitting is observed beyond fine structure. This additional splitting is known as hyperfine structure. The most significant contribution to hyperfine structure is the interaction of the nuclear magnetic moment with the magnetic field at the nucleus caused by the orbiting electron. The deviation of the nuclear charge distribution from a spherical shape offers a smaller contribution. The energy level splittings caused by hyperfine effects are smaller than the splittings associated with fine structure by about one to three orders of magnitude.

Hyperfine structure is characterized by the constants A_J and B_J, known as the magnetic dipole coupling constant and electric quadrupole coupling constant, respectively. As their names suggest, A_J describes the splitting caused by interaction of the nuclear spin to the magnetic field, while B_J describes the contributions from the quadrupole moment of the nuclear charge distribution. Both A_J and B_J can be measured experimentally or calculated.

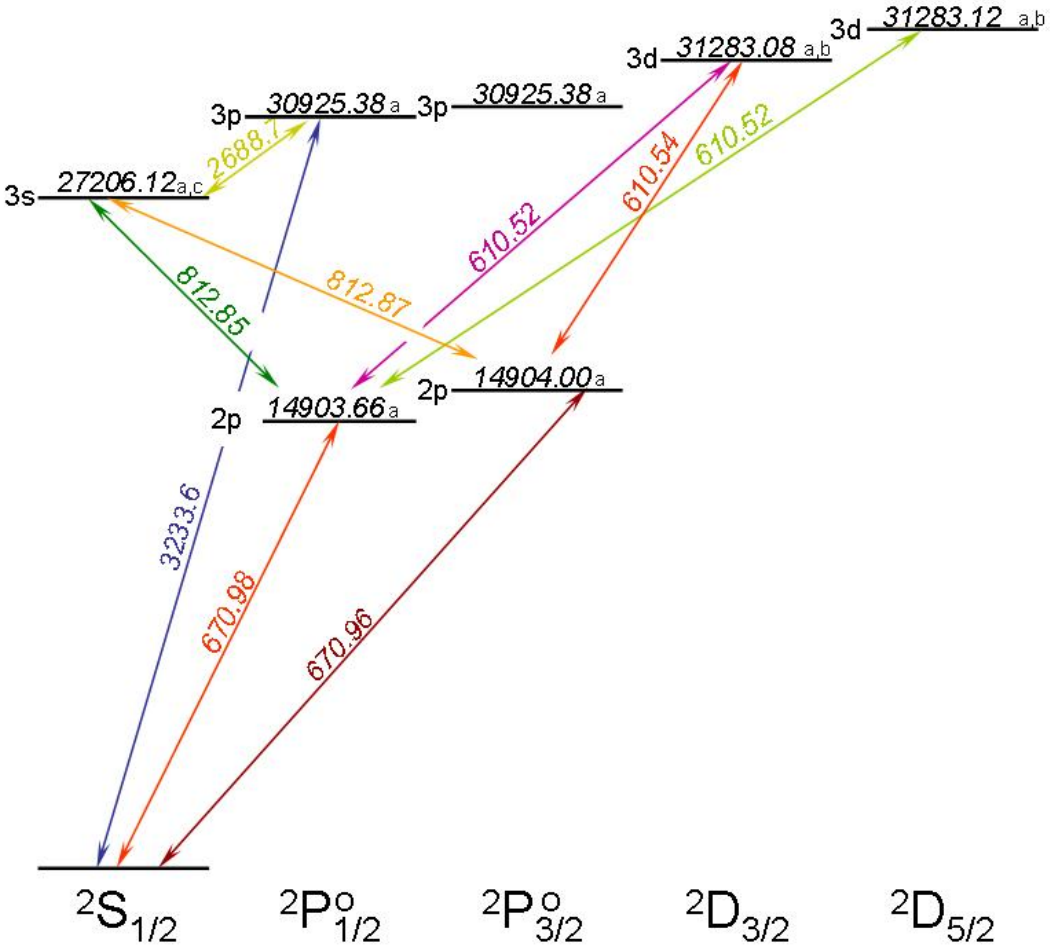

Figure 2.2: These lines represent the low-lying energy levels of lithium. Measurements labeled (a), (b), and (c) come from Refs. [21], [22] and [23], respectively.

2.5.1 Electric Dipole Interaction

Here we briefly outline the derivation of the contribution of the electric dipole interaction to the hyperfine energy level splitting. A more complete derivation can be found in Ref. [17].

Classically, the energy of a magnetic dipole moment in a magnetic field is given by [24]

$$U = -\vec{\mu} \cdot \vec{B}. \tag{2.44}$$

The energy of the nuclear magnetic moment in the electric field caused by the orbiting electrons can therefore be taken as a small perturbation to the Hamiltonian of the atom:

$$H_1 = -\vec{\mu}_I \cdot \vec{B}_{el}(0), \tag{2.45}$$

where μ_I is the nuclear magnetic moment. Since $\vec{\mu}_I$ is proportional to the intrinsic nuclear angular momentum, $\vec{I}$, and $\vec{B}_{el}(0)$ is proportional to $\vec{J}$ (as all vector quantities are proportional to angular momentum and point along the z-axis), Eq. 2.45 can be rewritten as

$$H_1 = A_J \vec{I} \cdot \vec{J}, \tag{2.46}$$

where A_J is the magnetic dipole coupling constant. As in Ref. [17], the energy splitting contribution from the electric dipole interaction is found to be

$$\Delta E_{md} = \frac{A_J}{2}[F(F+1) - I(I+1) - J(J+1)], \tag{2.47}$$

where $\vec{F} = \vec{I} + \vec{J}$. We see that the electric dipole interaction leads to splitting depending I and J. Additionally, Eq. 2.47 leads to F and M_F, the magnetic quantum number, being good quantum numbers, as the degeneracy of F has been lifted.

It important to note that Eq. 2.47 ignores the effect of J-J mixing in determining the relationship between hyperfine energy separations and the A_J coefficient. This effect

leads to significant corrections in determining the value of A_J for the P states of alkali metals. The corrections are particularly pronounced in ^{7}Li. See Ref. [25] for a detailed discussion of these corrections.

2.5.2 Electric Quadrupole Interaction

A smaller contribution to hyperfine structure arises from the nuclear charge distribution. Here we present the energy shifts caused by this effect. A derivation of this result can be found in Refs. [26].

The effect of the electric quadrupole coupling on energy levels can be determined by considering the electrostatic interaction given by

$$H_2 = -\sum_p \frac{e^2}{4\pi\epsilon_0|\vec{r}_e - \vec{r}_p|}, \tag{2.48}$$

where $\vec{r}_e$ and $\vec{r}_p$ are the positions of an electron and proton, respectively, relative to the center of mass of the nucleus, and where the sum is taken over the positions of all of the protons. The finite nuclear charge distribution is accounted for by assuming $r_e > r_p$. Then Eq. 2.48 can be expanded in powers of r_p/r_e, which yields a series of electric moments. The first term is the electric monopole moment. When it is summed over all protons and electrons, it gives the usual Coulomb interaction from a point-like nuclues. The second term in the series is the dipole term and from parity and time-reversal symmetry arguments, it can be shown that it is equal to zero. The next term is the electric quadrupole interaction. Following the usual multipole expansion, Eq. 2.48 can be written as

$$H_2 = \frac{1}{4\pi\epsilon_0}\sum_q (-1)^q Q_2^{-q}(n) F_2^q(e), \tag{2.49}$$

where Q_2^q and F_2^q denote the nuclear electric quadrupole tensor and electric field gradient tensor, respectively. Equation 2.49 can be simplified by defining the nuclear electric

quadrupole moment Q as

$$Q = \frac{2}{e}\langle I, M_I| \sum_j Q_2^0(p_j)|I, M_I = I\rangle, \tag{2.50}$$

where the sum is taken over all protons, and by writing the average of the gradient of the electric field as

$$\left\langle \frac{\partial^2 V_e}{\partial z^2} \right\rangle = \frac{1}{2\pi\epsilon_0}\langle J, M_J = J| \sum_i F_2^0(e_i)|J, M_J = J\rangle, \tag{2.51}$$

where the sum is over all electrons. With these introduced definitions, Eq. 2.49 takes the simplified form

$$H_2 = \frac{B_J}{2I(2I-1)J(2J-1)}(3(\vec{I}\cdot\vec{J})^2 + \frac{3}{2}(\vec{I}\cdot\vec{J}) - I(I+1)J(J+1)). \tag{2.52}$$

The expectation value of the perturbing quadrupole Hamiltonian is shown to be [26]

$$\Delta E_{eq} = \frac{B_J}{8I(2I-1)J(2J-1)}(3K(K+1) - (4I(I+1)J(J+1)), \tag{2.53}$$

where

$$K = F(F+1) - I(I+1) - J(J+1) \tag{2.54}$$

and

$$B_J = eQ\left\langle \frac{\partial^2 V_e}{\partial z^2} \right\rangle \tag{2.55}$$

is the electric quadrupole hyperfine coefficient. The total energy of any hyperfine state is therefore given by

$$\begin{aligned} E_{hf} &= E_{cog} + \Delta E_{md} + \Delta E_{eq} \\ &= E_{cog} + A_J\frac{K}{2} + B_J\frac{3K(K+1) - 4I(I+1)J(J+1)}{8I(2I-1)J(2J-1)}, \end{aligned} \tag{2.56}$$

where E_J is the center-of-gravity energy. Equation 2.56 allows us to see that in order for B_J to be nonzero, we must have $I \geq 1$ and $J \geq 1$.

In general, hyperfine corrections range from about one to three orders of magnitude smaller than those associated with fine structure. For less massive atoms, it can be difficult to resolve hyperfine structure for the P and D states because the natural linewidths of transitions can be comparable to hyperfine splitting. This is true of the D2 transition in lithium, which has a natural linewidth of about 6 MHz [27]. As shown in figure 2.1, the hyperfine splitting of the D2 transition is comparable to 6 MHz.

2.6 Energy Shifts and Splitting

The energy levels of an atom can be shifted and split in a number of different ways. For example, an external magnetic field will split the energy levels of an atom and a time-varying electric field will both split and shift energy levels. When performing high-precision measurements, as we are in this experiment, it is necessary to account for any effects that could shift the energy levels, so it is necessary to understand ac-Stark shifts and Zeeman splitting. In this section we discuss these two phenomena and provide an estimate of the ac-Stark shifts for this experiment.

2.6.1 Zeeman Splitting

When atoms are subject to an external magnetic field, the magnetic sublevels are split. This is known as the "Zeeman effect," and occurs because of the extra energy acquired by the atomic magnetic moment in the dc magnetic field. If the magnetic field is small, on the order of 10^{-3} T, then it can be regarded as a small perturbation,

$$H_1 = -\boldsymbol{\mu} \cdot \vec{B}. \tag{2.57}$$

As shown in Ref. [26], the energy shift due to this perturbation is

$$\Delta E = \langle \gamma \mathrm{L\ S\ J\ M_J} | -\boldsymbol{\mu} \cdot \vec{B} | \gamma \mathrm{L\ S\ J\ M_J} \rangle = g_J \mu_B B M_J, \tag{2.58}$$

where g_J is the Landé g-factor given by

$$\begin{aligned} g_J = g_l \left(\frac{J(J+1) + L(L+1) - S(S+1)}{2J(J+1)} \right) \\ + g_s \left(\frac{J(J+1) + S(S+1) - L(L+1)}{2J(J+1)} \right). \end{aligned} \tag{2.59}$$

Since $g_l = 1$ and $g_s \approx 2.0023$ [28], we can make the approximation that $g_s \approx 2g_l$. Then

$$g_J \approx \frac{3J(J+1) + S(S+1) - L(L+1)}{2J(J+1)}. \tag{2.60}$$

If the applied field is weak enough that the energy shift is less than the natural linewidth of the transition, then the lineshape is broadened [29].

2.6.2 ac-Stark Shift

When an atom is present in a time-varying external electric field, its energy levels will be split and shifted. This is known as the ac-Stark effect. Second-order time-independent perturbation theory is one method that can be used to arrive at the energy shifts. However, if we eschew the use of second-order time-independent perturbation theory, we can still arrive at approximately the same result by using the rotating wave approximation. In this section, we follow the derivation found in ref. [27].

Suppose we have an atom with two states, $|a\rangle$ and $|b\rangle$, with an energy separation of $\hbar\omega_0$. The atom is subjected to a time-varying electric field $\varepsilon_0 \sin(\omega_m t)$. We can treat the effect of the electric field as a weak perturbation so that the Hamiltonian of the system is

$$H = \begin{pmatrix} 0 & -d\varepsilon_0 \sin(\omega_m t) \\ -d\varepsilon_0 \sin(\omega_m t) & \hbar\omega_0 \end{pmatrix}. \tag{2.61}$$

Beginning with the time-dependent Schrödinger equation, we have

$$H|\psi\rangle = \imath\hbar \frac{\partial}{\partial t}|\psi\rangle. \tag{2.62}$$

We can then perform a unitary transformation by using the operator

$$U = \begin{pmatrix} 1 & 0 \\ 0 & e^{-\imath\omega_m t} \end{pmatrix}, \tag{2.63}$$

which yields

$$\begin{aligned} U^\dagger H U U^\dagger|\psi\rangle &= \imath\hbar U^\dagger \frac{\partial}{\partial t} U U^\dagger|\psi\rangle, \\ \left(U^\dagger H U - \imath\hbar U^\dagger \frac{\partial U}{\partial t}\right) U^\dagger|\psi\rangle &= \imath\hbar \frac{\partial}{\partial t} U^\dagger|\psi\rangle. \end{aligned} \tag{2.64}$$

Since the states are transformed as

$$|\psi'\rangle = U^\dagger|\psi\rangle, \tag{2.65}$$

we extract the "effective Hamiltonian," given by

$$\tilde{H} = U^\dagger H U - \imath\hbar U^\dagger \frac{\partial U}{\partial t}. \tag{2.66}$$

Plugging in the system Hamiltonian H, the effective Hamiltonian can be written explicitly as

$$\tilde{H} = \begin{pmatrix} 0 & -\frac{d\varepsilon_0}{2\imath}(1 - e^{-2\imath\omega_m t}) \\ \frac{d\varepsilon_0}{2\imath}(1 - e^{2\imath\omega_m t}) & \hbar\omega_0 \end{pmatrix} + \begin{pmatrix} 0 & 0 \\ 0 & -\hbar\omega_m \end{pmatrix}. \tag{2.67}$$

At this point, we invoke the rotating wave approximation, so that all quickly oscillating terms in the Hamiltonian drop out, i.e. $e^{2\imath\omega_m t}$ goes to zero. In this case, our effective Hamiltonian reduces to

$$\tilde{H} \approx \begin{pmatrix} 0 & -\frac{d\varepsilon_0}{2\imath} \\ \frac{d\varepsilon_0}{2\imath} & \hbar\omega_0 - \hbar\omega_m \end{pmatrix}. \tag{2.68}$$

This resembles a Hamiltonian corresponding to a dc Stark shift for a two level system with an energy separation of $\hbar(\omega_0 - \omega_m)$ in an applied electric field with magnitude $\frac{\varepsilon_0}{2}$. In the case of dc Stark shifts, energy level shifts are governed by

$$\Delta E = \sum_i \frac{d_{ik}^2 \varepsilon^2}{E_k - E_i}, \tag{2.69}$$

therefore the ac Stark shifts in our model atom are given by

$$\Delta E \approx \pm \frac{d^2 \varepsilon_0^2}{4\hbar(\omega_0 - \omega_m)}. \tag{2.70}$$

It is important to note that this approximation is only valid in the near-resonant case, when $\omega_m \approx \omega_0$. This is because we have neglected the finite linewidth of the transition.

2.7 Interaction of Atoms with Electromagnetic Radiation

The two basic ways by which photons interact with matter are absorption and emission. Here we present brief descriptions of these fundamental processes, as well as introduce the Wigner-Eckart theorem and relative transition amplitudes.

2.7.1 Absorption

When an atom interacts with a photon, there is some probability that it will absorb that photon and transition from a lower to a higher energy level. For this to occur, the energy of the photon must be equal to the difference in energy between the two states. The transition rate for absorption is proportional to the intensity of the radiation.

2.7.2 Spontaneous Emission

The complementary process of absorption is spontaneous emission, spontaneous meaning that the emission is not triggered by any external factor. If an atom is initially in an excited state and no radiation is present, then eventually it will naturally decay to a lower energy state and emit a photon.

In this experiment, the fluorescence we detect is produced by spontaneous emission. The average time that it takes for an atom to naturally decay from an excited state to a lower energy state is called the average lifetime of the transition. As a consequence of

the Heisenberg uncertainty principle, this results in an uncertainty in the energy of the transition given by

$$\Delta E \Delta T \approx \frac{\hbar}{2}. \tag{2.71}$$

This shows that the finite lifetime of a transition results in broadening of the spectral lineshape. The natural linewidth, often denoted by Γ, of a transition is extracted from this uncertainty in energy and describes the size of the broadening. In lithium, the average lifetime of the D1 and D2 transitions is ~ 27 ns and the natural linewidth is ~ 6 MHz [27].

2.7.3 Stimulated Emission

An incident photon can also cause an atom to drop from an excited state to a lower energy state. Under the influence of electromagnetic radiation, an atom has some probability to emit a photon with the same energy, direction and phase as the incident photon. As shown in Ref. [17], the rate of stimulated emission is equal to that of absorption. However, if population inversion occurs, that is if the system has more atoms in the excited state than in a lower energy state, then emission becomes the dominant process. This result is the basis for lasers and masers. A detailed discussion of lasers and masers can be found in Ref. [17].

2.7.4 The Wigner-Eckart Theorem

Many calculations in atomic physics involve the evaluation of matrix elements of tensor operators with respect to an angular momentum basis. These calculations can be simplified through application of the Wigner-Eckart theorem, which states that the matrix elements of an irreducible tensor operator T_q^κ (where κ is the rank of the tensor and the polarization $q = -\kappa, -\kappa + 1, ..., \kappa$) with respect to general angular momentum eigenstates

are given by [30]

$$\langle \gamma', F', M'_F | T^\kappa_q | \gamma, F, M_F \rangle = (-1)^{F'-M'_F} \langle \gamma', F' || T_\kappa || \gamma F \rangle \begin{pmatrix} F' & \kappa & F \\ -M'_F & q & M_F \end{pmatrix}, \tag{2.72}$$

where the reduced matrix element $\langle \gamma', F' || T_\kappa || \gamma F \rangle$ is independent of M_F, M'_F, and q, and is a property of the physical observable under consideration. The term in parentheses is a 3-j symbol. The 3-j symbol can be defined as the product of a Clebsch-Gordan coefficient and other numerical factors, and it obeys a number of symmetry relations [31]. For example, the 3-j symbol in Eq. 2.72 can be written as

$$\begin{pmatrix} F' & \kappa & F \\ -M'_F & q & M_F \end{pmatrix} = (-1)^{M'_F - F'} \frac{\langle F, M_F, \kappa, q | F', M'_F \rangle}{\sqrt{2F'+1}}. \tag{2.73}$$

This factor is determined by geometry and depends only on the orientation of the system relative to the z-axis.

To use the Wigner-Eckart theorem, the tensor operator must be expressed as an irreducible spherical tensor. As an example, we'll consider the dipole moment operator, $\vec{d}$. In Cartesian coordinates, the dipole operator is written as

$$\vec{d} = d_x \hat{x} + d_y \hat{y} + d_z \hat{z}. \tag{2.74}$$

This can be represented in the spherical basis defined by

$$\begin{aligned} \hat{e}_1 &= -\frac{1}{\sqrt{2}}(\hat{x} + i\hat{y}), \\ \hat{e}_0 &= \hat{z}, \\ \hat{e}_{-1} &= \frac{1}{\sqrt{2}}(\hat{x} - i\hat{y}), \end{aligned} \tag{2.75}$$

which yields

$$\begin{aligned} d_1 &= -\frac{1}{\sqrt{2}}(d_x + i d_y), \\ d_0 &= d_z, \\ d_{-1} &= \frac{1}{\sqrt{2}}(d_x - i d_y). \end{aligned} \tag{2.76}$$

Quantum Number	Description
L	Orbital angular momentum
S	Spin angular momentum
I	Nuclear spin
J	Total angular momentum, $\vec{J} = \vec{L} + \vec{S}$
F	Defined by $\vec{F} = \vec{I} + \vec{J}$
M_F	Magnetic quantum number

Table 2.1: Descriptions of various quantum numbers which, when paired with any other numbers needed to specify the state, form a coupled basis. The addition by which $\vec{F}$ and $\vec{J}$ are defined is an addition of vectors. This means that J and F take on integral values ranging from $|L-S|$ to $|L+S|$ and $|I-J|$ to $|I+J|$, respectively.

These are the components of an irreducible tensor operator with rank $\kappa = 1$ and for which $q = -1, 0, 1$, respectively [27]. The dipole operator is now expressed as an irreducible tensor operator. As we shall see in the next section, the Wigner-Eckart theorem can be applied to write the matrix elements of $\vec{d}$, expressed in some general angular momentum bases, as a product of reduced matrix elements and the Clebsch-Gordan coefficient.

2.7.5 Relative Transition Amplitudes

Different quantum numbers can be used to describe an atomic state. If appropriately chosen, the quantum numbers form a basis in which any atomic state can be represented. One basis, the coupled basis, uses the numbers L, S, I, J, F, M_F, and any other necessary quantum numbers, collectively referred to as γ, to specify an atomic state. These quantum numbers are summarized in table 2.1.

Suppose we have an initial state specified by $|i\rangle = |\gamma LSIJFM_F\rangle$ and a final state specified by $|f\rangle = |\gamma' L'S'I'J'F'M'_F\rangle$. The overall transition rate from $|i\rangle$ to $|f\rangle$ is determined by the full matrix element $\langle\gamma' L'S'I'J'F'M'_F|d_q|\gamma LSIJFM_F\rangle$, where d_q is the irreducible rank 1 tensor operator defined by Eqs. 2.76, and can be related to the reduced

matrix element through the Wigner-Eckart theorem. Invoking the theorem yields

$$\langle \gamma' L' S' I' J' F' M'_F | d_q | \gamma L S I J F M_F \rangle = (-1)^{F-M_F} \langle \gamma' L' S' I' J' F' || d || \gamma L S I J F \rangle \times \begin{pmatrix} F' & 1 & F \\ -M'_F & q & M_F \end{pmatrix}. \tag{2.77}$$

The reduced matrix elements on the righthand side of Eq. 2.77 can be written in terms of the uncoupled $|\gamma, L\rangle$ basis. Since the interaction Hamiltonian doesn't depend on I, we can relate reduced matrix elements in F to reduced matrix elements in J by decoupling I and J and using the uncoupled basis [30]:

$$\langle \gamma' L' S' I' J' F' || d || \gamma L S I J F \rangle = (-1)^{J+I+F+1} \langle \gamma' L' S' J' || d || \gamma L S J \rangle \times \sqrt{(2F+1)(2F'+1)} \begin{Bmatrix} J' & F' & I \\ F & J & 1 \end{Bmatrix}, \tag{2.78}$$

where the term in curly braces is a "Wigner 6-j symbol[1]." We can use this tactic again to relate reduced matrix elements in J to reduced matrix elements in L by decoupling L and S, and the result is

$$\langle \gamma' L' S' I' J' F' || d || \gamma L S I J F \rangle = (-1)^{2+L'+S'+2J+I+F} \langle \gamma' L' || d || \gamma L \rangle \times \sqrt{(2F+1)(2F'+1)(2J+1)(2J'+1)} \times \begin{Bmatrix} J' & F' & I \\ F & J & 1 \end{Bmatrix} \begin{Bmatrix} L' & J' & S' \\ J & L & 1 \end{Bmatrix}. \tag{2.79}$$

Since the reduced matrix element $\langle \gamma' L' || d || \gamma L \rangle$ is the same for all hyperfine sublevels and fine structure levels of the D1 and D2 transitions for lithium, the transition rate W_{if}, for a

[1]The Wigner 6-j symbols are real numbers that possess a number of symmetry properties. For example, they are invariant under any permutations of the columns and are invariant under interchange of the upper and lower rows [32]. A more detailed discussion of Wigner 6-j symbols can be found in Ref. [30].

given polarization q, from state $|i\rangle$ to state $|f\rangle$ satisfies

$$W_{if} \propto (2F+1)(2F'+1)(2J+1)(2J'+1) \times \begin{Bmatrix} J' & F' & I \\ F & J & 1 \end{Bmatrix}^2 \begin{Bmatrix} L' & J' & S' \\ J & L & 1 \end{Bmatrix}^2 \begin{pmatrix} F' & 1 & F \\ -M_F' & q & M_F \end{pmatrix}^2, \tag{2.80}$$

Equation 2.80 can be used to calculate the relative probabilities of different transitions. If an ensemble of atoms obeying Boltzmann statistics is being considered then the ground states will all be equally populated. This causes the atoms to fill the F states according to the number of M_F states and therefore changes the relative strength of the transition. This can be accounted for by multiplying Eq. 2.80 by $2F+1$.

This example shows the power of the Wigner-Eckart theorem. It allowed us to express the the matrix elements of an irreducible tensor operator as a product of real coefficients (the 3-j symbol and phase factor) and a reduced matrix element that depends on the dipole operator. By decoupling I and J, and then L and S, we were able to further simplify the reduced matrix elements. These steps have converted a complicated problem into a trivial calculation. In this case, the reduced matrix elements can actually be looked up in a table, for example in Ref. [27].

2.8 Doppler Shift

Consider laser light propagating in the $\vec{k}$ direction. Now suppose a beam of atoms is directed to intersect with the laser perpendicular to $\vec{k}$. This is a typical setup in atomic spectroscopy experiments. If the atoms travel perfectly perpendicular to the laser beam, then all of the atoms will observe the same frequency for the laser light. However, it is typically not true that all of the atoms will intersect perfectly perpendicular to the beam, that is the beam will not be perfectly collimated. Any mechanism that produces an atomic

beam will usually result in some angular spread of the atoms as they travel away from the source. The atoms will assume a range of velocities v_t transverse to the ideal direction of the atomic beam. As a result, the frequencies observed by these atoms are Doppler shifted according to

$$\nu = \nu_0 \left(1 + \frac{v}{c}\right). \tag{2.81}$$

In this experiment, an atomic beam is directed perpendicular to a probe laser beam. However, as the atoms travel across the width of the laser beam, they spread out along the direction parallel to the propagation direction of the laser. As a result, they observe Doppler shifted frequencies of the laser light. Since the natural linewidth of the D1 and D2 transitions in lithium are less than the Doppler shifts (see Secs. 2.7.2 and 6.4.3), reducing the effects of Doppler broadening leads to increased resolution of the transitions.

2.9 Retroreflection

In an attempt to further decrease the effects of the Doppler width, the laser beam is retroreflected. When the laser frequency is not exactly on resonance (figure 2.3b), atoms from separate velocity classes will, due to Doppler shifts, will observe the same frequencies of light. As a result, two velocity classes will contribute to the fluorescence spectrum when the laser is slightly detuned from the atomic transition. On the other hand, when the laser is resonant with the transition (figure 2.3a), only atoms that travel perpendicular to the laser will contribute to the spectral lineshape. In the resonant case, there will be fewer atoms contributing to the fluorescence signal. This is reflected as a small dip in the lineshape. See figure 2.4.

The technique of retroreflection aids in compensating for Doppler broadening as it allows for greater resolution of atomic transitions.

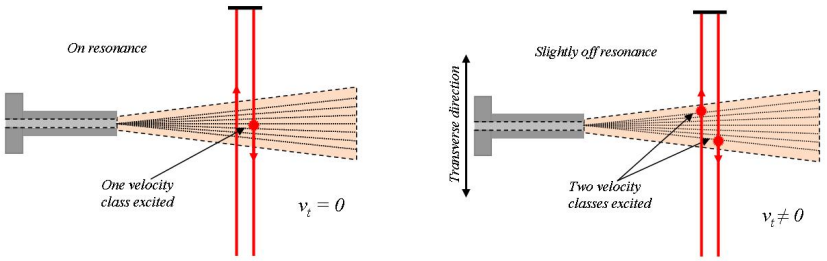

(a) When the laser is on resonance, one velocity class is excited.

(b) When the laser is off resonance, multiple velocity classes are excited.

Figure 2.3: When the laser is slightly detuned from the transition frequency (figure 2.3b), two separate transverse velocity classes will contribute to the fluorescence signal. When the laser is on resonance (figure 2.3a), only the zero transverse velocity class contributes. This results in a small dip in the spectral lineshape.

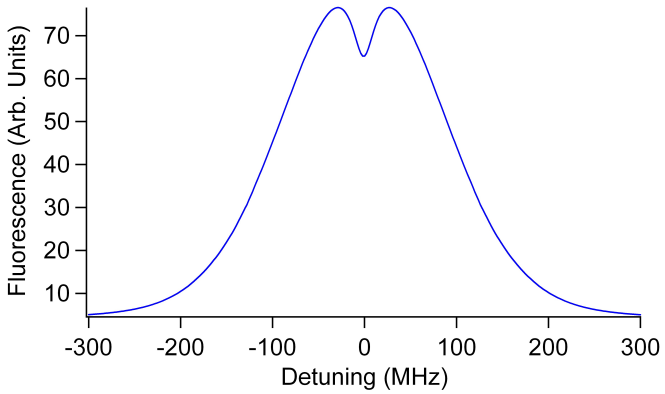

Figure 2.4: This sample lineshape shows a saturated fluorescence dip that appears in a calculated spectrum for a two-level system. The code used to produce this spectrum can be found in appendix 1.

2.10 The Density Matrix

In this section, we introduce the density matrix. This is a tool that is useful in modeling statistical ensembles of quantum systems, for example, atoms. In this work, the density matrix is used to calculate the spectral lineshape of lithium.

2.10.1 A Generalized Wave Function

The wave function is limited in the types of ensembles that it can describe. An ensemble of quantum systems, such as a group of atoms, can be characterized by a single wave function only if the ensemble is completely coherent. However, if the ensemble consists of quantum systems that do not share the same phase relationship, then any description that uses a single wave function is rendered ineffective.

The density matrix is a generalization of the wave function that enables one to describe ensembles that cannot be characterized by a single wave function. It can be used to describe populations that are incoherent, or partially coherent. Just as the Schrödinger equation is used to determine the time evolution of single atoms or pure ensembles, the Liouville equation governs the temporal development of mixed ensembles. Furthermore, the time evolution of the density matrix can be modified to include terms that account for "relaxation" and "repopulation," or in other words, the interaction of the ensemble with the environment. Some mechanisms that cause relaxation are collisions between atoms and radiative decay of atoms in excited states. Processes that lead to repopulation include the entrance of atoms into the interaction region and optical pumping. The density matrix is therefore very useful in modeling atomic physics experiments, in which the subject of study is often an ensemble of (not necessarily coherent) atoms.

In the present experiment, we use the density matrix to model the time evolution of the population of lithium atoms entering and exiting the interaction region. By varying

phenomenological terms in the time evolution of our density matrix, the effects of polarization angle, optical pumping, and external electric and magnetic fields can be further understood. This allows for a more thorough understanding of the observed spectra.

In the subsequent sections, we follow derivations presented in Ref. [32].

2.10.2 The Density Operator and Matrix

Suppose we have an ensemble containing N quantum systems. If we perform a measurement, then there is some observable A that represents the measurement. The value of the measurement is the expectation value of A averaged over the N atoms in the ensemble. We can write this as

$$\overline{\langle A \rangle} = \frac{1}{N} \sum_{i=1}^{N} \langle \psi_i | A | \psi_i \rangle \,. \tag{2.82}$$

We can insert the identity operator

$$\hat{I} = \sum_{j} |\phi_j\rangle \langle \phi_j| \,, \tag{2.83}$$

where $\{|\phi_j\rangle\}$ is any complete set of basis vectors, into the above equation to obtain

$$\begin{aligned} \overline{\langle A \rangle} &= \sum_{j} \frac{1}{N} \sum_{i=1}^{N} \langle \psi_i | A | \phi_j \rangle \langle \phi_j | \psi_i \rangle \\ &= \sum_{j} \frac{1}{N} \sum_{i=1}^{N} \langle \phi_j | \psi_i \rangle \langle \psi_i | A | \phi_j \rangle \\ &= \sum_{j} \langle \phi_j | \frac{1}{N} \sum_{i=1}^{N} |\psi_i\rangle \langle \psi_i | A | \phi_j \rangle \,. \end{aligned} \tag{2.84}$$

Applying the definition of the trace of an operator,

$$\mathrm{Tr}(B) = \sum_{j} B_{jj} = \sum_{j} \langle \phi_j | B | \phi_j \rangle \,, \tag{2.85}$$

we obtain

$$\overline{\langle A \rangle} = \mathrm{Tr} \left(\frac{1}{N} \sum_{i=1}^{N} |\psi_i\rangle \langle \psi_i| \, A \right). \tag{2.86}$$

If we define the density matrix to be

$$\rho = \frac{1}{N}\sum_{i=1}^{N} |\psi_i\rangle \langle\psi_i| , \tag{2.87}$$

then Eq. 2.84 condenses to

$$\overline{\langle A\rangle} = \mathrm{Tr}(\rho A). \tag{2.88}$$

The elements of the density operator form the density matrix. The entries in the density matrix are given by

$$\rho_{ij} = \langle\phi_j|\rho|\phi_k\rangle = \frac{1}{N}\sum_{i=1}^{N} \langle\phi_j|\psi_i\rangle \langle\psi_i|\phi_k\rangle = \frac{1}{N}\sum_{i=1}^{N} c_j^{(i)} c_k^{(i)*}, \tag{2.89}$$

where $c_j^{(i)}$ and $c_k^{(i)}$ are the jth and kth expansion coefficients of state ψ_i. The off-diagonal ($j \neq k$) elements represent the coherence between states ϕ_j and ϕ_k. On the diagonals ($j = k$) of the density matrix, we have

$$\rho_{jj} = \frac{1}{N}\sum_{i=1}^{N} |c_j^{(i)}|^2, \tag{2.90}$$

and accordingly, these entries represent the average probability of finding one of the quantum systems in the state ϕ_j, which is a state held by a population.

2.10.3 The Liouville Equation

Just as the Schrödinger equation can be used to describe the time evolution of a single atom or an ensemble of coherent atoms, the Liouville equation, coupled with the initial conditions of the ensemble and the environment, determines the evolution of the density matrix. Let us begin by explicitly computing the time derivative of the density matrix:

$$\begin{aligned} i\hbar\frac{d}{dt}\rho &= i\hbar\frac{1}{N}\sum_{i=1}^{N}\frac{d}{dt}|\psi_i\rangle\langle\psi_i| \\ &= \frac{1}{N}\sum_{i=1}^{N}\left(\left(i\hbar\frac{d}{dt}|\psi_i\rangle\right)\langle\psi_i| + |\psi_i\rangle\left(i\hbar\frac{d}{dt}\langle\psi_i|\right)\right). \end{aligned} \tag{2.91}$$

At this point, we may apply the Schrodinger equation

$$i\hbar\frac{d}{dt}\left|\psi_i\right\rangle = H\psi_i \tag{2.92}$$

to obtain

$$i\hbar\frac{d}{dt}\rho = \frac{1}{N}\sum_{i=1}^{N}\left(H\left|\psi_i\right\rangle\left\langle\psi_i\right| - \left|\psi_i\right\rangle\left\langle\psi_i\right|H\right), \tag{2.93}$$

but this is just the commutator of H and ρ, so we have

$$i\hbar\frac{d}{dt}\rho = [H,\rho]. \tag{2.94}$$

This is known as the Liouville equation, and it is used to determine how the density matrix evolves in time. The time evolution is determined solely by the initial conditions of the system. Terms that account for interactions with the environment are built into the Hamiltonian.

2.10.4 Relaxation

The Liouville equation (Eq. 2.94) describes the time evolution of quantum systems, e.g., atoms, whose only interactions are described by the Hamiltonian. This is a simplifying assumption that significantly limits the Liouville equation's utility in describing atomic physics experiments. Atoms in a vacuum chamber can collide with each other and with the walls of the vacuum chamber. Even when collisions are ignored, atoms interact with the quantum vacuum by spontaneously emitting radiation, thereby decaying to a lower energy state. These interactions, collision and emission, are "relaxation processes" because they bring the system, the ensemble of atoms, back towards thermal equilibrium.

Relaxation processes can be reflected in the Liouville equation by including additional terms. Here, we present a short derivation of the relaxation term, following Ref. [32].

Atoms that are initially in an exited state will spontaneously decay. Though the mechanisms of relaxation vary, the net effect of spontaneous decay of an atomic state $|\phi_j\rangle$

can be represented by subtracting a term from the right-hand side of Eq. 2.94. If the decay is assumed to be exponential at a rate of $\Gamma_j/2$, then the relaxation of this population of atoms can be described as

$$\frac{d}{dt}\rho_{jj} = -\Gamma_j \rho_{jj}, \tag{2.95}$$

which means that the average probability of finding an atom in state $|\phi_j\rangle$ decreases exponentially. Relaxation also affects the coherences. The rate of change of a coherence is just the average of the decay rate for each state:

$$\frac{d}{dt}\rho_{ij} = -\frac{(\Gamma_i + \Gamma_j)}{2}\rho_{ij}, \qquad i \neq j. \tag{2.96}$$

If we introduce a relaxation matrix Γ, whose elements are defined by Eqs. 2.95 and 2.96, then a compact relaxation term can be included on the right-hand side of the Liouville equation:

$$i\hbar\frac{d}{dt}\rho = [H, \rho] - i\hbar\frac{1}{2}(\Gamma\rho + \rho\Gamma). \tag{2.97}$$

To account for different mechanisms of relaxation, the decay rates in the relaxation matrix can include separate terms corresponding to each relaxation process.

2.10.5 Repopulation

As a complement to relaxation, repopulation processes describe the filling of states of the system. States can be filled by transfer of populations from one state to another. For example, when atoms undergo radiative decay from one state to a lower energy state, the lower state is repopulated. Repopulation also occurs when "new" atoms are introduced to the system. One mechanism for the introduction of atoms to the system is the entrance of atoms into the interaction region of the laser and the atomic beam. Of course, as atoms enter the interaction region, other atoms leave, and so the number of atoms in the system remains roughly the same.

Repopulation is incorporated into the Liouville equation in a way similar to that of relaxation. For example, if the repopulation term describes unpolarized atoms that enter the interaction region, then the introduced atoms will be equally likely to repopulate any of the ground state sublevels. If there are n ground state sublevels and the transit rate of the atomic beam is γ, then we can define a repopulation matrix Λ that has ground state terms of $\frac{\gamma}{n}$ and is zero everywhere else. Like the relaxation term, the repopulation term is also added to the right-hand side of the Liouville equation:

$$i\hbar\frac{d}{dt}\rho = [H,\rho] + i\hbar\Lambda. \tag{2.98}$$

There are many mechanisms of repopulation, and accordingly, there are a variety of repopulation terms that could be added to the right-hand side of the Liouville equation.

2.10.6 Steady State Solutions

The steady state solution of a system is determined by specifying that $\frac{d\rho}{dt} = 0$, so that the solution is constant in time. If we use representative relaxation and repopulation terms $-i\hbar\frac{1}{2}(\Gamma\rho + \rho\Gamma)$ and $i\hbar\Lambda$, then solutions to the equation

$$i\hbar\frac{d}{dt}\rho = [H,\rho] - i\hbar\frac{1}{2}(\Gamma\rho + \rho\Gamma) + i\hbar\Lambda = 0 \tag{2.99}$$

are the steady state solutions of the system.

2.10.7 The Fluorescence Operator

In this experiment, we detect the fluorescence produced by atoms that decay from excited states to lower states by spontaneous emission. To see how this phenomenon is built into density matrix calculations, we consider a density matrix in an excited state ρ_{mn}; it will decay by spontaneous emission to a lower state ρ_{ij}. In this case, the rate of change of

the lower state is given by[2] [32]

$$\dot{\rho}_{ij} = \sum_{m,n} \frac{4}{3} \frac{\omega_{ni}^3}{\hbar c^3} \vec{d}_{im} \cdot \vec{d}_{nj} \rho_{mn} \quad = \sum_{m,n} F_{ij}^{mn} \rho_{mn}, \tag{2.100}$$

where we have introduced the fluorescence operator

$$F_{ij}^{mn} = \frac{4}{3} \frac{\omega_{ni}^3}{\hbar c^3} \vec{d}_{im} \cdot \vec{d}_{nj}. \tag{2.101}$$

Summing over upper indices, we obtain

$$\dot{\rho} = \mathrm{Tr} \rho F. \tag{2.102}$$

We can understand the components of Eq. 2.100 qualitatively. Classically, an oscillating dipole moment, $\vec{d}(t) = \vec{d} \sin \omega t$ emits radiation at a rate given by

$$I = \frac{2\omega^4}{3c^3} \vec{d} \cdot \vec{d}. \tag{2.103}$$

We can divide the righthand side of this equation by the energy of a photon, $\hbar\omega$, to find the rate per photon:

$$\frac{2\omega^3}{3\hbar c^3} \vec{d} \cdot \vec{d}. \tag{2.104}$$

This equation is similar in form to Eq. 2.100, which can be considered the quantum mechanical analog.

2.10.8 Counterpropagation

As noted in Sec. 2.9, we retroreflect the beam to perform saturated fluorescence spectroscopy. This is an important effect that can be built into density matrix calculations. As an example, we consider a two level system given by states

$$|a\rangle = \begin{pmatrix} 1 \\ 0 \end{pmatrix} \text{ and } |b\rangle = \begin{pmatrix} 0 \\ 1 \end{pmatrix}. \tag{2.105}$$

[2]CGS units are being used in Eq. 2.100 and through the rest of this subsection.

For a light wave propagating in the positive x direction, the electric field as a function of position and time is given by

$$E(x,t) = \varepsilon_0 e^{i(kx-\omega t)}. \tag{2.106}$$

If the beam is retroreflected, then the electric field becomes a superposition of the wave propagating in the positive x direction and one propagating in the opposite direction, so that

$$\begin{aligned} E(x,t) &= \varepsilon_0 e^{i(kx-\omega t)} + \varepsilon_0 e^{i(-kx-\omega t)} \\ &= \varepsilon_0 e^{-i\omega t}\left(e^{ikx} + e^{-ikx}\right) \\ &= \varepsilon_0 e^{-i\omega t}(2\,\cos(kx)). \end{aligned} \tag{2.107}$$

As the spatial portion of Eq. 2.107 is time independent, this is the equation of a standing wave.

Since there is generally some divergence to atomic beams, the standing wave picture does not hold for all of the atoms. Since the atomic beam is not perfectly collimated, atoms from different areas of the beam will have different velocities relative to the direction of propagation of the laser. The atoms' velocities parallel to the laser, v_x, are described by a Doppler distribution centered at $v_x = 0$. As a result, only the atoms that travel perfectly perpendicular to the laser will interact with a stationary electric field. The electric field experienced by an atom with velocity v_x along the direction of the laser beam propagation is then

$$\begin{aligned} E(v_x,t) &= \varepsilon_0 e^{-i\omega t}\,\cos(k(v_x t + x_0)) \\ &= \varepsilon_0 e^{-i\omega t}\,\cos(kv_x t + \phi). \end{aligned} \tag{2.108}$$

The Hamiltonian for the two level system subject to this external field can then be constructed as

$$H = \begin{pmatrix} 0 & d\varepsilon_0 e^{-i\omega t} 2\,\cos(kv_x t + \phi) \\ d\varepsilon_0 e^{-i\omega t} 2\,\cos(kv_x t + \phi) & \hbar\omega_0 \end{pmatrix}. \tag{2.109}$$

To calculate the spectrum resulting from a two-level system interacting with a counterpropagating beam, the Liouville equation (Eq. 2.94) must be solved using the above Hamiltonian. Solutions must be calculated for different values of v_x, and additionally, they must be averaged over various phases ranging from 0 to 2π so that solutions do not preferentially select a particular phase.

Chapter 3

Experimental Setup

In this chapter, we present the important information about the components of this precision measurement experiment. In particular, the frequency comb, diode laser, vacuum chamber, lithium oven, and data collection procedures are discussed.

A diagram of the experimental setup is shown in Fig. 3.1. The frequency of the diode laser is stabilized to a particular mode of the comb. The laser light is coupled into a single-mode fiber, to give the beam a Gaussian profile, and then retroreflected across the atomic beam. The frequency of the rf signal generator that controls the repetition rate of the comb is adjusted, and thus the frequency of the diode laser. Since we know f_0, f_r, and f_b to a high level of precision, we can easily determine the absolute frequency of the diode laser is controlled.

3.1 Frequency Comb

In this experiment, we used an optical frequency comb to stabilize the frequency of our diode laser. In the frequency space picture, as shown in Fig. 3.2, the optical frequency comb is a set of equidistantly spaced spectral lines. The frequencies present in a frequency

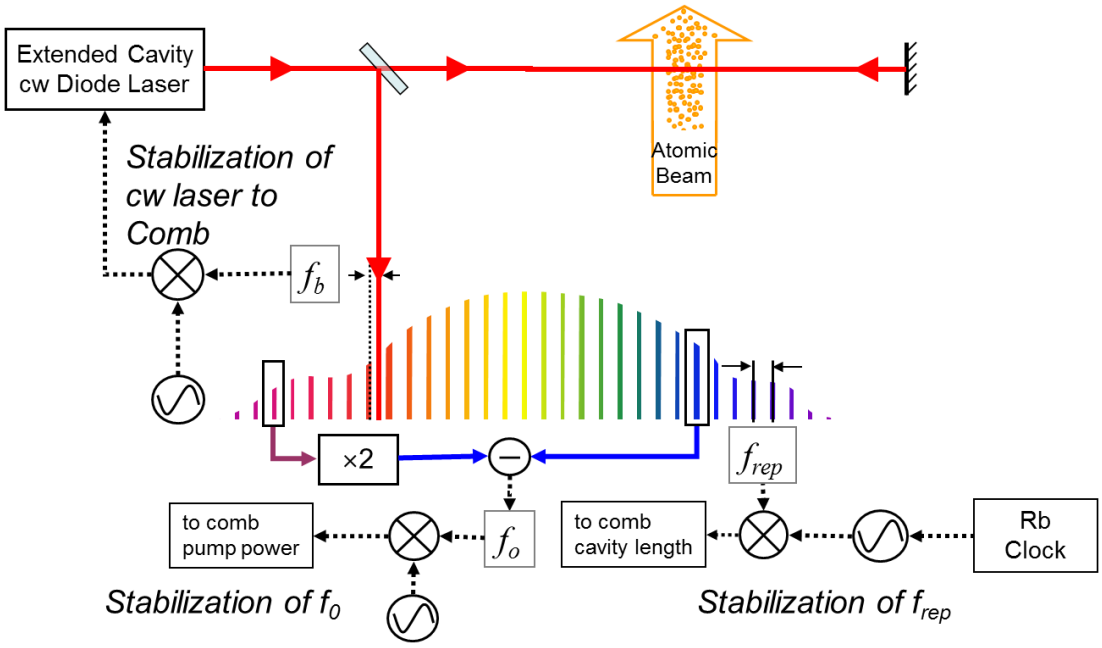

Figure 3.1: Our experimental setup. The diode laser is frequency stabilized and retroreflected through the atomic beam.

comb are determined by the offset frequency, f_0, the mode number, n, and the repetition rate, f_{rep}. Mathematically, the relationship is known as the comb equation:

$$\nu = f_0 + n f_{rep}. \tag{3.1}$$

The frequency comb is produced using a Ti:Sapphire laser. The frequency comb contains $\sim 4 \times 10^5$ modes with a spacing of ~ 950 MHz [33].

3.1.1 Ti:Sapphire Oscillator

A titanium-doped sapphire crystal with an absorption coefficient of $\alpha = 6.56$ at 514 nm acts as the gain medium. To control the temperature of the crystal, it is mounted in a piece of copper that is connected to a solid-state temperature control unit manufactured by ThermoTek. The circulating water is kept at $\sim 20^\circ$ C.

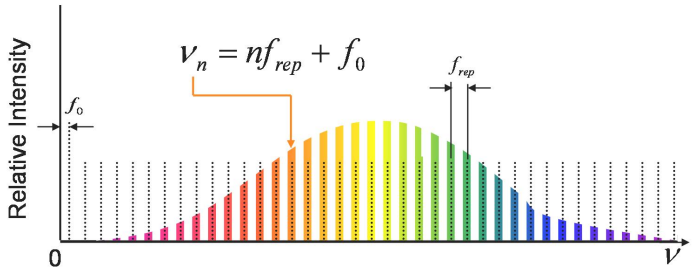

Figure 3.2: In the frequency domain, the frequency comb is a collection of evenly spaced frequencies. Any frequency in the comb is given by $f = f_0 + nf_{rep}$.

The Ti:Sapphire crystal is pumped with a frequency-doubled ND:$YV0_4$ 'Verdi' laser operating at 532 nm, and it is manufactured by Coherent. Typical operating powers run from 5.0 to 5.5 W.

The setup for our frequency comb is similar to the "Standard Ti:Sapphire" resonators discussed in Ref. [34]. The cavity, or "optical resonator," is arranged in a bowtie configuration, as displayed in Fig. 3.3. It consists of four mirrors, a lens and a crystal. The effective cavity length is $\sim$ 30 cm, which translates to a repetition rate of $\sim$ 950 GHz, or about $\sim$ 1 ns between pulses. The output coupling (OC) mirror is 99% reflective, while mirrors M1, M2 and M3 are chirped to compensate for group velocity dispersion. Mirrors M1 and M2 are curved mirrors with radii of curvature equal to 3 cm. The two mirrors have group velocity dispersion (GVD) of -70 fs^2, and work together as a dispersion-compensated pair. Mirror M3 is a plane mirror with a GVD of -40 fs^2. Mirror M3 is attached to a piezo ceramic element. By adjusting the voltage to the piezo ceramic, the cavity length can be controlled, which allows for fine adjustments of the repetition rate. Mirror M2 is mounted on a micrometer translation stage, allowing for alignment of the cavity. The resonator is housed in a 10 cm $\times$ 20 cm $\times$ 30 cm box, as pictured in Fig. 3.4.

A number of parameters can be adjusted to achieve lasing and mode-locking. In particular, the angles and positions of the mirrors, the pump power, crystal position, and

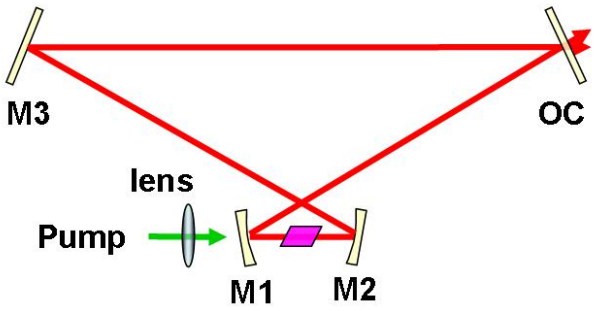

Figure 3.3: The optical resonator is arranged in a bowtie configuration. The crystal, pictured in purple, is located between mirrors M1 and M2. Mirrors M1, M2 and M3 are chirped to compensate for group velocity dispersion. The output coupling (OC) mirror is 99% reflective. The length of the cavity, that is the total distance covered by the laser in one round trip of the cavity, is $\sim$ 30 cm. Picture from Ref. [35].

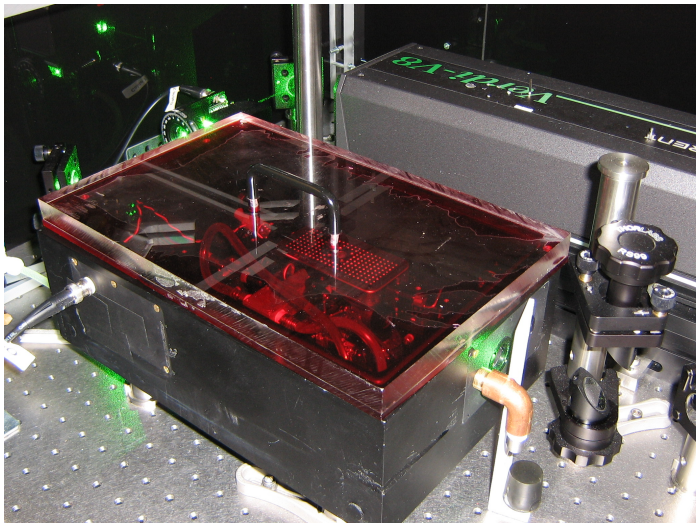

Figure 3.4: The resonator is housed in a 10 cm $\times$ 20 cm $\times$ 30 cm box. The 'Verdi' pump laser can be seen behind the resonator housing.

crystal angle can all be varied (see Fig. 3.3). Once alignment of the optical elements has achieved lasing within the cavity, the position of M2 is adjusted by use of a translation stage to produce conditions that are conducive to mode-locking. To accomplish mode-locking, an external perturbation must be introduced in order to disrupt the stability of the beam propagating within the cavity. This is is done by gently tapping mirror M2 with the handle of a screwdriver.

Once mode-locked, the pulses can travel in only one direction, though the direction of propagation is arbitrary. There are a few tactics that can be used to determine whether mode-locking has been achieved. One is to observe whether one or two spots are output by the cavity. When the laser operated in CW mode, the crystal emits light in both directions, but when when mode-locked, light propagates in only one direction, so the presence of only one spot indicates that mode-locking has been achieved. The visual appearance of the beam also changes depending on whether it is mode-locked. When in CW operation, the beam has a granular, speckled quality, an interference effect resulting from the spatially coherent laser light and small variations in path length difference caused by the roughness of the surface reflecting the light. When mode-locked, the spot has a dull quality. Depending on the desired mode, the alignment is adjusted until the the laser is mode-locking in the correct direction. The output power of the laser is ~ 550 mW when mode-locked.

Stabilization and detection of the offset frequency requires that the comb spans an optical octave, meaning that the frequency of the highest mode must be greater than twice the frequency of the lowest mode; this is explained more thoroughly in Sec. 3.1.3. The output spectrum generated by the Ti:Sapphire laser does not regularly span an optical octave, so we use an air-silica microstructure fiber to achieve the required broadening. The fiber is made of a lattice of air-holes in fused silica. The air-holes result in anomalous dispersion that cancels out the normal dispersion caused by the silica. For further discussion

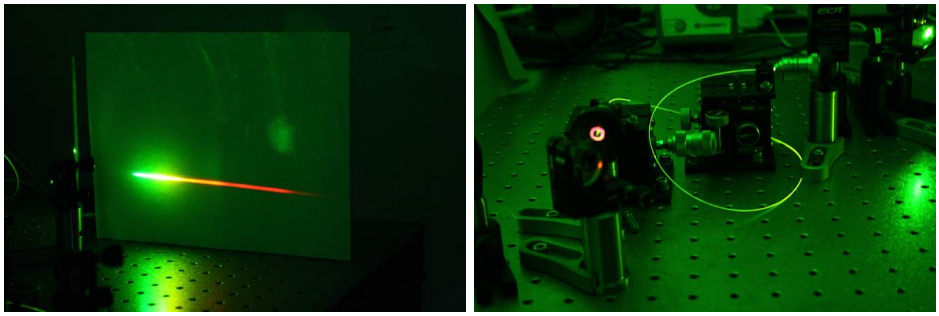

(a) Output Spectrum **(b)** Micro-structured Fiber

Figure 3.5: Output spectrum (a) after broadening in a nonlinear fiber (b). The spectrum ranges from 450 nm to 1100 nm, covering the visible frequencies and a small part of the infrared spectrum.

of this effect, see Ref. [36]. Figure 3.5a shows the output spectrum of our comb after broadening in a nonlinear fiber. A more detailed discussion of the setup and stabilization of the frequency comb can be found in Refs. [29, 35, 37].

3.1.2 Detection, Control, and Stabilization of f_{rep}

To detect f_{rep}, part of the comb laser is picked off and sent to a fast photodiode (Electro-Optics Technology ET-2030A amplified silicon detector). We control f_{rep} by adjusting the length of the cavity. This is achieved through a feedback loop that controls the voltage applied across a piezo ceramic. Laser light from the comb is broadened in a microstructure fiber and sent through a 600 nm short pass filter, and then sent to a fast photodiode. The incident light contains f_{rep} as well as the higher harmonics $2f_{rep}, 3f_{rep}, ...$ because the many modes present in the comb interfere and produce beat frequencies that are multiples of f_{rep}. However, since the detector range is less than 1.5 GHz, harmonics higher than $2f_{rep}$ are not present in the output signal of the detector. To filter out unwanted signals, the output of the detector is sent through a bandpass filter. It is then sent to an rf mixer where it is combined with a signal generated by a synthesizer that is referenced to a

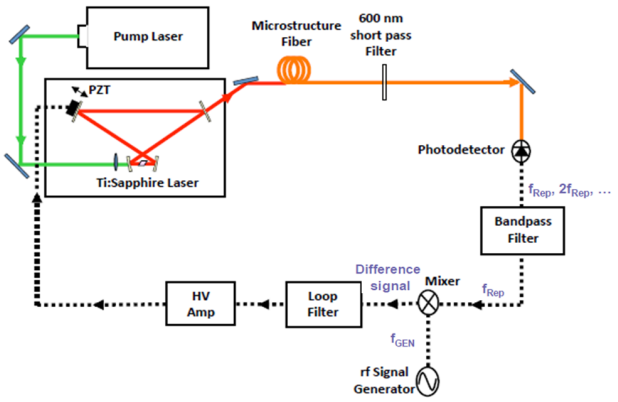

Figure 3.6: Block diagram of the f_{rep} stabilization setup. Picture from Ref. [37].

GPS-steered rubidium atomic clock. The mixer outputs the difference signal between f_{rep} and the synthesizer frequency, also known as the error signal. The error signal is passed through a loop filter which shapes it so that the piezo will respond as desired. The output of the loop filter feeds into a high voltage amplifier which drives the piezo ceramic. The particular piezo ceramic we use is a Noliac CMAR03 PZT [1]. The piezoelectric ceramic, attached to M3 (see Fig. 3.3), is therefore controlled by the feedback loop, as pictured in Fig. 3.6.

3.1.3 Detection, Control, and Stabilization of f_0

Detection of f_0 is more complicated than for f_{rep}. It requires that the frequency comb spans an optical octave, meaning that it contains a lower frequency $\nu_1 = n_1 f_{rep} + f_0$ and a higher frequency $\nu_2 = n_2 f_{rep} + f_0$, where $n_2 = 2n_1$. The lower frequency ν_1 can be doubled and heterodyned with ν_2 to extract f_0, as shown in Fig. 3.7.

As mentioned in Sec. 3.1.1, an optical octave is produced by passing the comb light

[1] PZT stands for lead zirconate titanate. It is a type of piezoelectric material.

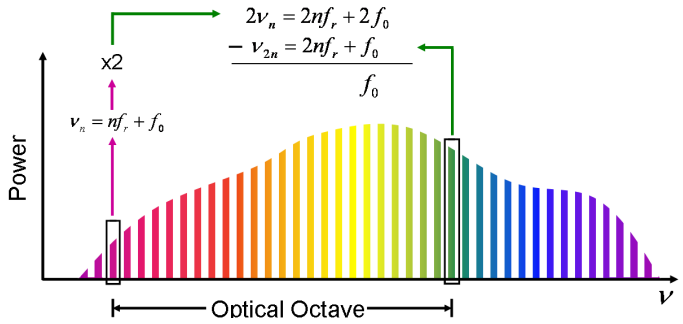

Figure 3.7: To detect f_0, a lower frequency ν_1 and higher frequency ν_2 are beat against each other. Detection of f_0 requires that the comb spans an optical octave.

through a microstructure fiber (see. Fig. 3.8. The frequencies present in the optical octave range from 530 nm (green) to 1060 nm (infrared). Frequency doubling of the lower frequency infrared light is achieved using a periodically poled lithium niobate (PPLN) crystal. The crystal is designed to frequency double light with a wavelength of $\sim$ 1064 nm. Two pulses, one composed of frequencies originally near 530 nm and the other composed of the frequency doubled light, are heterodyned on the photodetector. However, the dispersion from various optical elements introduces a time delay between the pulses. To account for this phase lag, a cold mirror that reflects light with a wavelength between 420 and 630 nm but transmits light with a wavelength between 750 and 1200 nm is used to separate the 530 nm and 1060 nm light and send each of the beams to high-reflectance mirrors before recombining and passing through the doubling crystal. The position of one of the mirrors is variable. The path length difference introduced by this splitting and recombining of the beams can be adjusted by varying the position of the mirror. Judicious adjustment of the mirror position compensates for the time delay.

A 530 nm bandpass filter is placed after the doubling crystal to isolate the light originally at 530 nm and the frequency doubled light originally near 1060 nm. The two beams interfere and are incident on a photodetector. There is ambiguity as to the sign of

f_0, as it is the beat frequency produced by the interference two different frequencies of light. As such, f_0 is the absolute value of the difference of two frequencies:

$$f_0 = |\nu_2 - \nu_1|. \tag{3.2}$$

In other words, it is not clear whether the green light directly produced in the fiber or the frequency doubled green light has the higher frequency. Correctly determining the sign of f_0 is critically important in determining absolute frequencies and can be done by checking that the sign is consistent with observed fluorescence spectra, as discussed in Sec. 3.1.6. It is also important to note that the frequency doubled light will still interfere with comb modes that have made it through the bandpass filter. As a result, the beam incident on the fast photodiode will contain not only f_0, but $|f_0 \pm f_{rep}|, |f_0 \pm 2f_{rep}|, |f_0 \pm 3f_{rep}|$, etc.

The offset frequency can be controlled by adjusting the pump power. As a result of the nonlinear dependence of dispersion in the Ti:Sapphire crystal, a change in pump power results in a change in f_0. The pump power can be varied by passing the beam through an acousto-optic modulator (AOM). The AOM consists of a crystal attached to a piezoelectric transducer. Applying an rf voltage across the piezeoelectric transducer produces lattice vibrations (phonons) that scatter the incident light. This deflects the light so that it does not couple into the laser cavity. The amount of scattering is proportional to the applied rf power.

The offset frequency is stabilized with a phase lock similar to the one used for f_{rep}. However, the noise on f_0 is much greater than the noise on f_{rep}. The repetition rate drifts by ~ 100 Hz over a few minutes. In the same time, the offset frequency changes by 5 to 10 MHz. To account for the increased noise, a number of steps are taken to extend the capture range of the electronics.

As previously mentioned, the beam incident on the fast photodiode contains a

number of other frequencies in addition to f_0, and as a result they are present in the output signal of the detector. A bandpass filter is used to remove these unwanted signals. The output signal is then combined with the signal from an atomic-clock-referenced rf generator so that the sum is 1240 MHz; for example, if the output signal were 300 MHz, we would set the rf generator to 940 MHz. The resulting signal is passed through a divide-by-8 circuit to increase the capture range of the phase lock. After passing through the circuit, the signal has a frequency of 1240 MHz/8 = 155 MHz. A second rf signal generator, also referenced to the atomic clock, is used to mix-down the signal with a digital phase detector. The resulting error signal is shaped with a loop filter and sent to an rf generator which drives the AOM. The relationship between the sign of the error signal and the appropriate response of the pump power is unclear; a positive error signal does not necessarily indicate that the pump power should be decreased, and likewise a negative error signal does not necessarily suggest that power should be increased. To account for this ambiguity, an invert switch on the loop filter can be flipped to change the sign of the error signal.

The repetition rate is generally more stable than the offset frequency. During data collection, maintaining the f_0 lock requires frequent adjustments to the pump power and carrier level of the rf driver.

3.2 Diode Laser

While the frequency comb provides us with an absolute frequency, the power in any one mode of the comb is too little to produce measurable resonance signals. Instead, we use an extended cavity diode laser that is frequency stabilized to a particular mode of the comb.

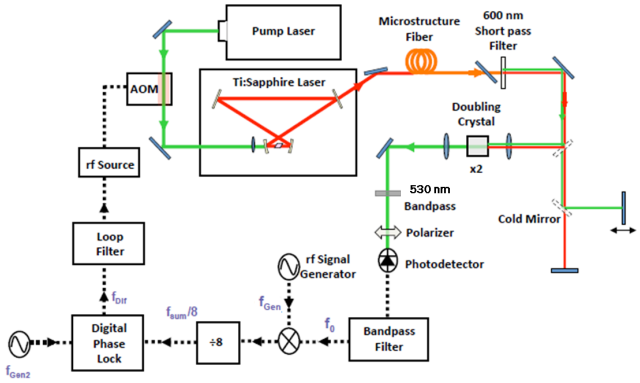

Figure 3.8: Block diagram of the f_0 stabilization setup. Picture from [37].

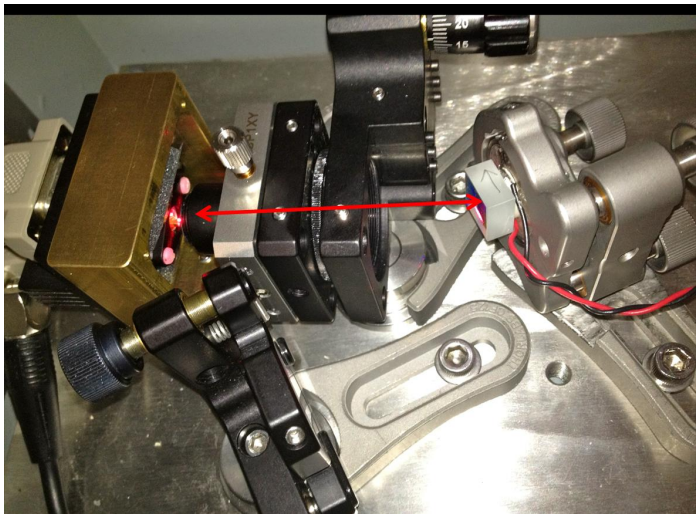

Figure 3.9: Our Diode laser, mounted in the Littrow configuration. The red double-headed arrow indicates the extent of the laser cavity. The diode is on the left and the diffraction grating is on the right. By adjusting the angle of the diffraction grating, we control the wavelength at which the ECDL lases. The length of the cavity is modulated through the application of a voltage across a piezo ceramic.

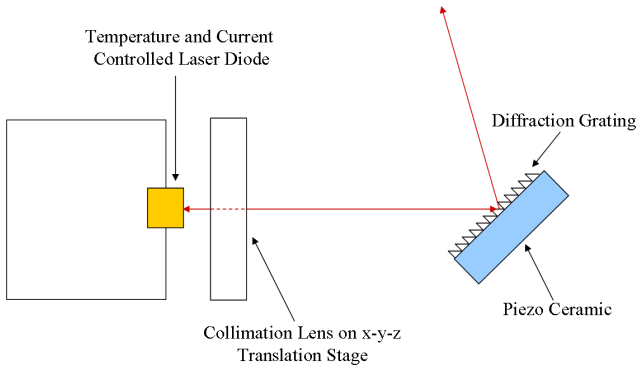

Figure 3.10: Diagram of our ECDL oriented in the Littrow configuration. Adjusting the angle of the grating relative to the incident beam allows us to select the correct frequency for excitation of atomic resonances. To scan over the resonances, the cavity length is modulated by application of a voltage across the piezo ceramic. A lens mounted on the $x-y-z$ translation stage allows for further alignment of the ECDL.

3.2.1 Extended Cavity Diode Laser Setup

In this experiment, our diode laser is mounted in the Littrow configuration, as shown in Fig. 3.10. The injection current and temperature of the laser diode are controlled with a ThorLabs LCD205C current controller and TED200C temperature controller, respectively. A collimation lens mounted on an $x-y-z$ translation stage allows for tuning and alignment of the diode laser. The diffraction grating has 1800 grooves/mm and is attached to a piezo ceramic and mounted on a Polaris Low Drift Kinematic Mirror Mount. The separation distance between the diode and diffraction grating is ~ 7 cm.

Adjusting the angle of the diffraction grating allows us to select the correct wavelength. Adjusting the voltage across the piezo changes the length of the cavity thereby allowing us to scan over resonances of the lithium atoms.

3.2.2 Anti-Reflective Coating

In this experiment, we use an AlGaInP laser diode manufactured by Hitachi, and we have applied anti-reflective (AR) coating to it. Without AR coating, commercially purchased laser diodes are not ideal candidates for single-mode lasers because their tuning ranges (via adjustments to the temperature and injection current) are very limited, they exhibit multi-mode behavior, are sensitive to optical feedback, and are generally unstable. However, through the application of AR coating, commercially available diodes can be modified to produce single-mode, narrow linewidth light. The use of AR coated diodes in conjunction with external cavity feedback leads to significant gains in terms of tuning range, stability, and having a narrow linewidth [38]. In this experiment, we have AR coated our diode following the procedure outlined in Ref. [39].

To AR coat our diodes, we first remove the can of the laser diode with a hand-held ThorLabs diode laser can opener. In a vacuum chamber operating at $\sim 10^{-7}$ Torr, a layer of silicon oxide is evaporated so that it deposits on the laser diode. The output power of the diode is monitored; a decrease in the power output by the diode indicates that the coating is reducing the cavity feedback. Coating continues until the power of the diode laser stop decreasing and starts increasing, at which point a metal shutter is rotated into place to prevent the further deposition of the coating material. Figure 3.11 shows the power output of the diode laser as a function of current, with optical feedback, before and after coating.

3.2.3 Frequency Stabilization of the Diode Laser

The frequency of the diode laser is stabilized using the setup shown in Fig. 3.12. The diode laser and the filtered beam from the frequency comb are passed through a polarizing beamsplitting cube, giving the two beams orthogonal polarizations. A polarizer placed after the beamsplitting cube and oriented at $\sim 45^{\circ}$ projects the polarization of the

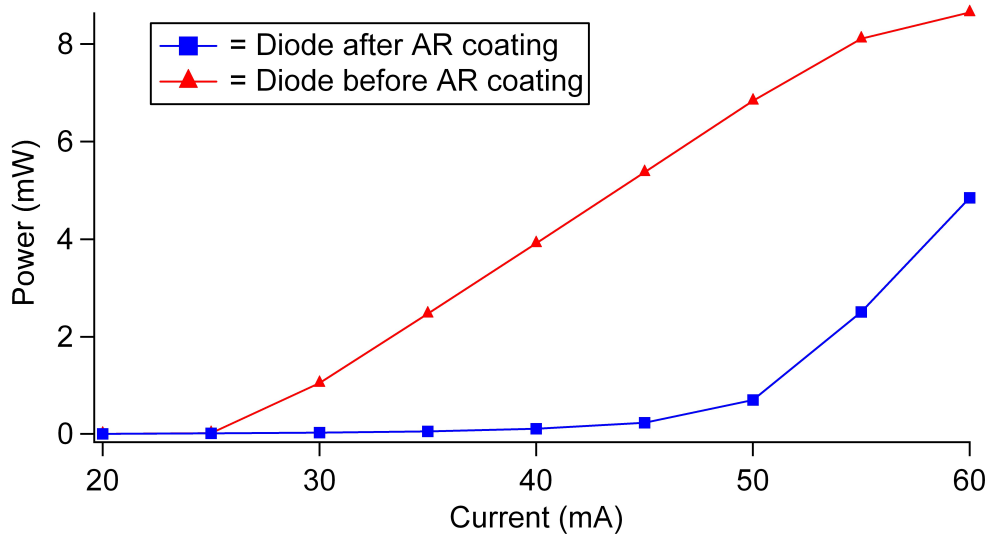

Figure 3.11: Power of diode laser with external feedback before (red) and after (blue) AR coating.

two beams onto a single axis. The diode and the comb beams are heterodyned; this signal is monitored with a fast photodiode. A bandpass filter selects one of them and then the signal is mixed up to 1240 MHz using an rf signal generator. Similar to the stabilization of f_0, this signal is sent to a divide-by-16 circuit[2]. Not pictured in Fig. 3.12, the signal is then sent to a 1240 MHz bandpass cavity filter. Using a second rf signal generator, the signal is mixed down. The output, which is close to zero, serves as the error signal. A resistor-divider network controls the current feedback.

The injection current provides high frequency ($\sim$ 150 kHz) feedback while the diffraction grating gives low frequency ($\sim$ 1 kHz) feedback. The grating feedback signal is sent to a loop filter and then a high voltage amplifier which provides the voltage across the piezo ceramic to which the grating is attached.

[2]In this case, a divide-by-16 is used in place of a divide-by-8 circuit because there is more noise on the diode laser signal than on the f_0 signal.

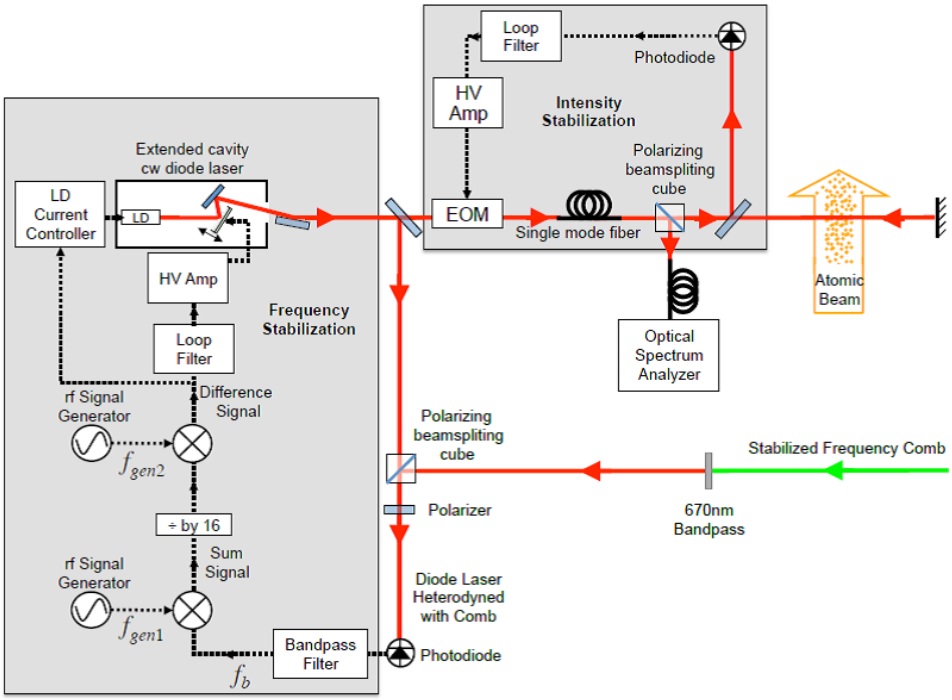

Figure 3.12: ECDL frequency stabilization setup. Diagram taken from Ref. [29].

3.2.4 Fabry-Perot Interferometer

The Fabry-Perot interferometer is useful in a number of applications. For example, it has been used in the analysis of hyperfine spectral structure, determination of the index of refraction of gases, and the calibration of the standard meter in terms of wavelengths [40]. It can also be used to check whether a laser is operating single-mode, which is how it is used in this experiment.

3.2.4.1 Planar-Planar and Confocal Fabry-Perot Cavities

A planar-planar Fabry-Perot cavity consists of two partially reflective mirrors oriented parallel to one another and separated by some distance, as shown in Fig. 3.13. The incident beam enters the cavity and then reflects off of a mirror. Since the mirrors are only partially reflective, some of the light is transmitted while the rest continues to reflect between the inner surfaces of the two mirrors, with part of the beam exiting the cavity whenever it is reflected by one of the mirrors, allowing the beam to interfere with itself many times within the cavity. If the cavity length is such that the beam produces standing waves between the mirrors, then the Fabry-Perot interferometer will transmit light, otherwise it will interfere destructively and no light will get through. The condition for constructive interference of the parallel beams is

$$2d\,\cos(\theta) = m\lambda, \tag{3.3}$$

where d is the separation distance between the two mirrors, θ is the angle of the incident beam relative to the optical axis of the system, m is an integer, λ is the wavelength of the light, and we are assuming that air with an index of refraction $n = 1$ fills the space between the mirrors. The Fabry-Perot cavity can therefore be used to test whether a beam is of a single-frequency. If the wavelength of a single-mode incident beam is modulated

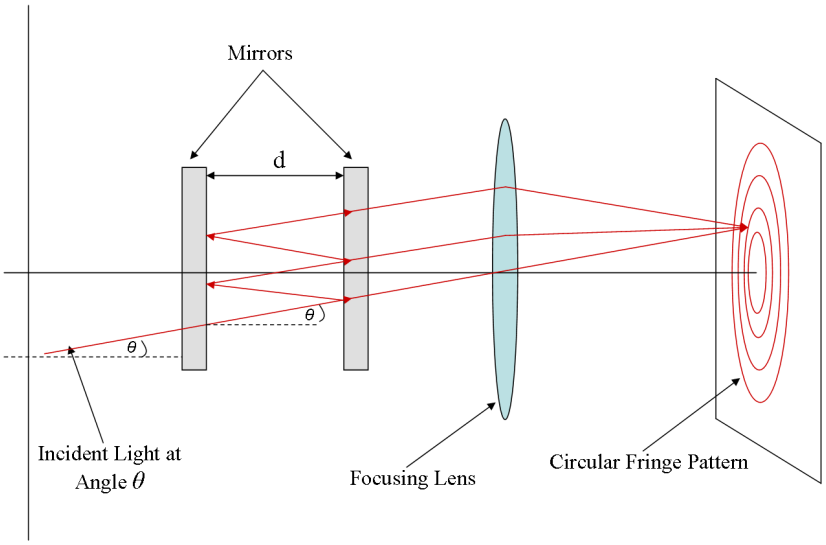

Figure 3.13: Diagram of a planar-planar Fabry-Perot interferometer.

at a constant rate, then it will produce an interference maximum when the condition for constructive interference (Eq. 3.3) is met, which will be at regularly spaced intervals in time.

An alternative version of the Fabry-Perot interferometer consists of two spherical mirrors, each with a radius of curvature equal to the length of the cavity, as pictured in Fig. 3.14. One advantage of the confocal Fabry-Perot cavity is that it is much easier to align than, for example, a cavity with parallel planar mirrors. The spacing between successive transmission peaks, or the free spectral range (FSR) of a confocal Fabry-Perot interferometer is given by

$$FSR = \frac{c}{4L}, \tag{3.4}$$

where L is the length of the cavity.

The Fabry-Perot cavity can provide valuable information about the character of a

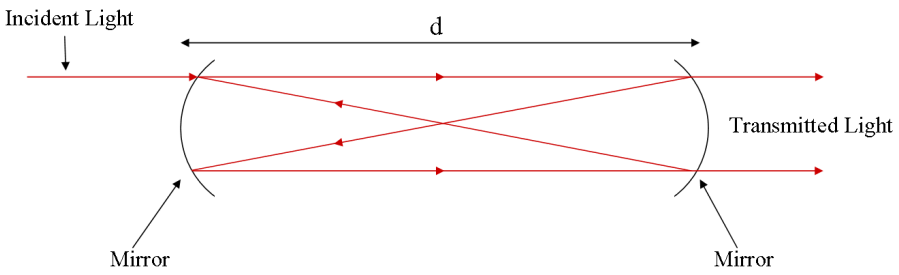

Figure 3.14: Diagram of confocal Fabry-Perot interferometer.

beam. In this experiment, we used a confocal Fabry-Perot cavity to check whether the diode laser was exhibiting single-mode behavior and to determine the range of frequencies over which it would remain stable. This was done by applying a $\sim$ 60 Hz triangle wave to the piezo ceramic, thereby modulating the cavity length of the ECDL. Transmission through the Fabry-Perot was monitored with a photodiode. The FSR of our Fabry-Perot cavity is 250 MHz.

Ideally, in the transmission lineshape of our Fabry-Perot interferometer, we like to see a number of peaks evenly spaced by 250 MHz over a large scan range, i.e. a large modulation ($\sim$ 3 GHz) of the ECDL frequency. This would indicate that the ECDL is operating as a single-mode laser. If the spacing of the Fabry-Perot transmission peaks is irregular, this indicates that the laser is mode hopping. Single-mode behavior can be optimized by careful alignment of the ECDL. In Fig. 3.15, an example plot of Fabry-Perot transmission peaks shows a case in which the operation of the laser is single-mode over $\sim$ 1.5 GHz. However, there is also some irregularity in the spacing of the peaks, indicating that there is some drift in the frequency of the laser.

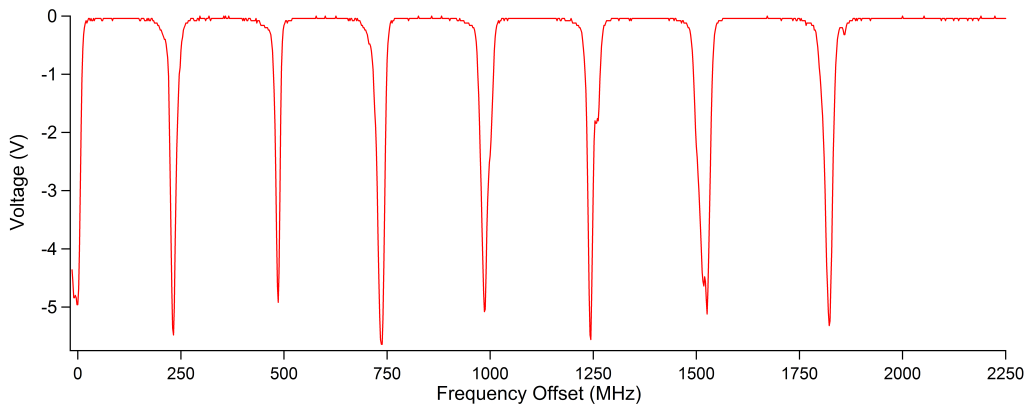

Figure 3.15: The output of the Fabry-Perot Cavity.

3.2.5 Optical Spectrum Analyzer

In our experiment, we use laser light at a specific frequency to excite energy transitions in lithium. We use the optical spectrum analyzer (OSA) as a tool to calibrate the frequency of our diode laser. We use a beam splitting cube to separate a small fraction of the beam and couple it into a multi-mode fiber that feeds into the OSA. We use a multi-mode fiber before feeding into the OSA mainly due to the ease of coupling the beam through multi-mode as opposed to single-mode fiber. The OSA displays the power as a function of wavelength and allows us to adjust the alignment of the diode laser so that it outputs light with a wavelength of 670.94 nm.

In practice, we use the OSA only as a rough diagnostic of the wavelength. After adjusting the alignment of the laser cavity grating so that the OSA indicates that the wavelength of our beam is 670.94 nm, we do not usually observe fluorescence signal. However, this results in an alignment that is close to producing the correct wavelength, and so we proceed to make fine adjustments to the alignment while checking for fluorescence signals directly, via the output from the PMT. When our laser is on resonance, the OSA consistently reads closer to 671.12 nm, so there appears to be some offset to the measurements

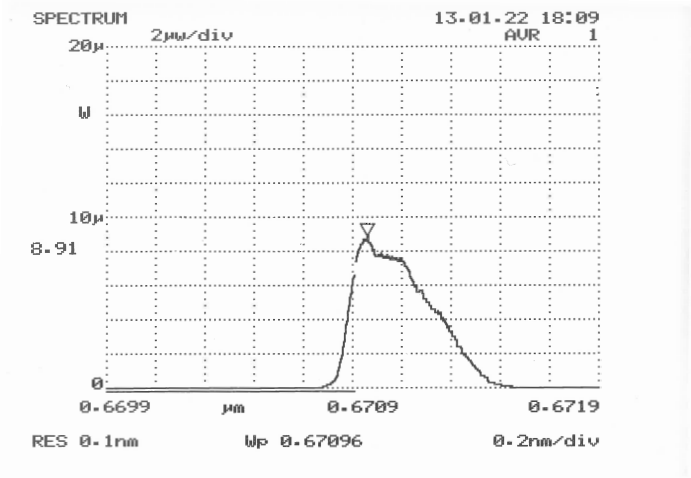

Figure 3.16: Typical output of the optical spectrum analyzer. The asymmetry displayed on the OSA is an artifact of the machine and does not reflect the character of our beam.

of the OSA. Also, the OSA indicates that our beam profile is heavily asymmetric. Even when we coupled a single frequency He:Ne laser into the OSA, the asymmetry was present, which indicates that this is an artifact of the machine rather than our beam. See Fig. 3.16 for the raw output of the OSA.

3.2.6 Power Stabilization

To compensate for natural fluctuations in the power of the diode laser, we use an electro-optic modulator (EOM) to actively stabilize the power. Here we discuss how EOMs work and the explain the power stabilization feedback loop used in the experiment.

In some crystals, the index of refraction depends on the value of the local electric field. By applying a voltage across a crystal, the index of refraction along one of the axial directions can be varied. If light that is polarized at some angle relative to the y-axis propagates through the crystal, then the polarization will be rotated by an amount depending on the index of refraction of the crystal which is a function of the applied voltage [41]. The light then passes through a polarizing beam splitter. The power output by either

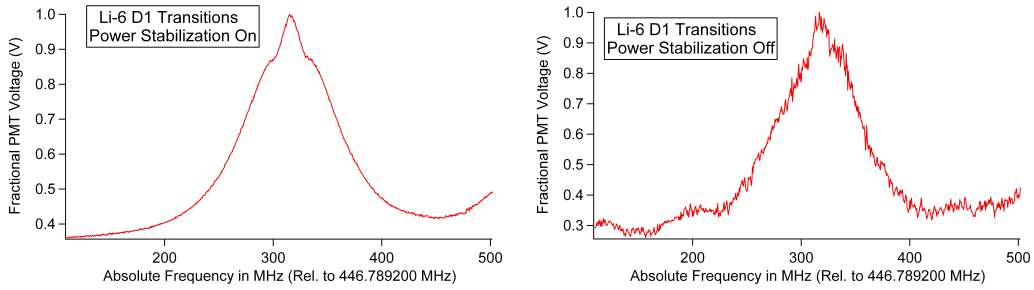

(a) Power Stabilization On **(b)** Power Stabilization Off

Figure 3.17: Fluorescence spectra with (a) and without (b) power stabilization. The power stabilized data offer significantly increased resolution of the transition.

arm of the beamsplitter will change depending on the polarization angle of the incident light. Since the EOM controls the polarization of the incident light, it controls the power that is sent to the interaction region.

In our experiment, we monitor the power of the diode laser by splitting off a small fraction of the light before it enters the interaction region and sending it to a photodiode. This signal is sent to a loop filter and compared to a stable dc voltage. The signal is sent from the loop filter to a high voltage amplifier which amplifies the signal before it is sent to the EOM. This feedback loop is shown in Fig. 3.12.

For comparison, data collected with and without active power stabilization are shown in Fig. 3.9. The power stabilization leads to a much less noisy signal and allows for greater resolution of the spectral lineshape.

3.3 Vacuum Chamber

The atomic beam and the laser interact in high-vacuum, typically around 10^{-7} Torr when the oven is heated. The vacuum chamber consists of a 4.50" expanded spherical cube designed by Kimball Physics, various bellows, and an ion pump. The ion pump is

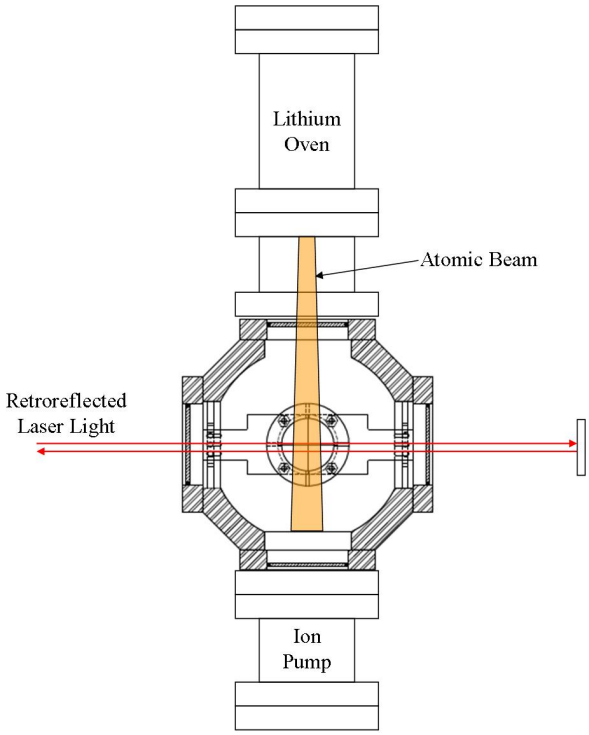

Figure 3.18: Schematic of the top view of the vacuum chamber. The atomic beam and laser light interact toward the center of the spherical cube. The laser light enters and exits the vacuum chamber through windows in bellows (not shown) that are attached to the sides of the spherical cube. Fluorescence is detected by a PMT that is mounted on the top of the spherical cube.

capable of achieving pressures as low as 10^{-11} Torr, but the system must be pumped for a great period of time and baked to achieve such pressures.

The interaction region is located near the center of the spherical cube. The lithium oven is connected to one side of the cube while the laser enters through an adjacent window. The PMT is fastened to the top window. See Fig. 3.18 for a schematic of the vacuum chamber.

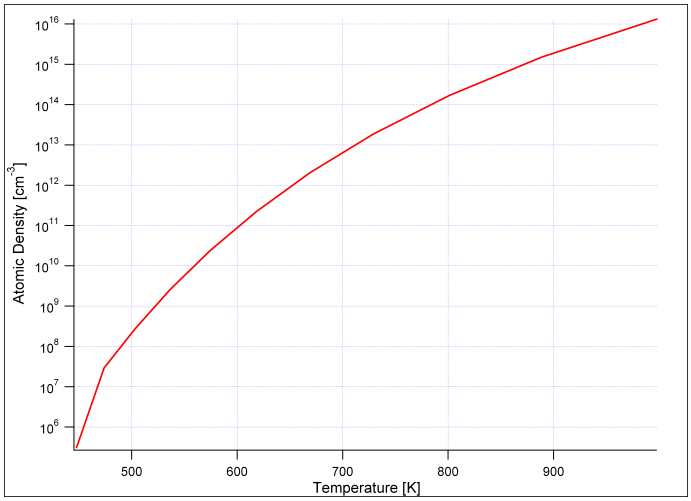

Figure 3.19: Vapor pressure curve for lithium. In this experiment, the atoms are heated to $\sim 350°$ C, which corresponds to a density of about 10^{12} atoms/cm^3 inside the oven.

3.4 Atomic Lithium Beam

The atomic beam is produced by heating lithium in a stainless steel oven. The melting point of lithium is 180° C, but we usually heat the oven to $\sim 350°$ C [42]. Heating the lithium to this temperature gives us, according to the vapor pressure curve for lithium, an atomic density of $\sim 10^{12}$ atoms/cm^3 (see Fig. 3.19).

3.4.1 Oven

The oven is made of a stainless steel 2 1/8" diameter standard conflat nipple. Threaded rods, which attach the oven to the vacuum chamber, are welded to a blank flange which is welded to the back end of the oven. Another blank flange with a diameter of 0.5" is welded to the front of the oven. The nozzle is bolted so it can be removed, allowing us to refill the oven once it has been depleted of lithium. For a schematic of the lithium oven, see Fig. 3.20.

The oven is heated by tantalum heater wire. The tantalum wire is wound into a

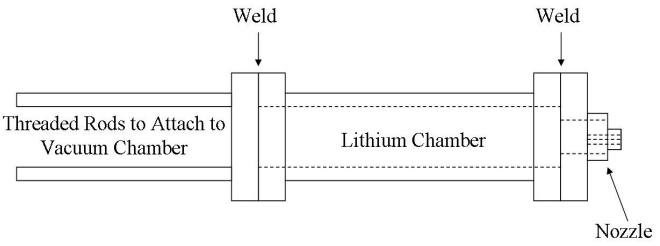

Figure 3.20: A schematic of the lithium oven. Dotted lines indicate holes. The front flange is welded shut and the nozzle is bolted, rather than welded, to the front of the oven; this allows us to remove the nozzle and load the oven with lithium. Two heat shields (not pictured) surround the oven.

tight coil and then gently stretched and passed through ceramic tubing to prevent shorting. One heater surrounds the outside of the lithium chamber while another makes contact with the nozzle. The body heating elements are held in place with stainless steel wire, while the nozzle heater is fixed by a blank flange that is screwed into the front flange of the oven. The nozzle is heated to prevent lithium from solidifying and clogging the nozzle. The heating of the lithium chamber and nozzle is controlled independently by two Variacs, which apply voltage across the heater wires. To prevent the radiative dissipation of heat, two thin sheets of stainless steel have been curved to enclose the chamber region. We measure the temperature by use of two type-k thermocouples. They are placed on the outside of the oven, one at the front and the other at the back. As a result, the temperature that we measure is only a rough estimate of the actual temperature of the lithium atoms. We have measured temperature differences as large as $\sim 50^\circ$ C between the front and back thermocouples, yet we have found that the average of these two measurements is consistent with the amplitudes of the observed signals, see Sec. 3.7.

3.4.2 Nozzle

The heated lithium atoms leave the oven through a nozzle machined from stainless steel, pictured in Fig. 3.22. Seven 0.5" long .0595" diameter sections of a stainless steel hypodermic needle are inserted into the central channel of the nozzle to produce a highly collimated atomic beam, increasing the beam density and thus the amplitudes of the observed signals. Previously, a longer nozzle was used (see Fig. 3.21a). The intention was to produce an even more collimated beam, however, we rarely observed any fluorescence signals when the long nozzle was in place. After spending a considerable deal of time searching for signals, with limited success, the short nozzle was reinstated, and fluorescence signals were observed soon thereafter. Initially, we suspected that the longer may have led to clogging, but before switching back to the short nozzle, the lithium oven and nozzle were cleaned and reloaded, and the nozzle heater was fastened securely. Still, we did not observe signals. Another possibility for this difficulty could have been the alignment of the atomic beam and the laser; we have found that even with the short nozzle, the alignment is very sensitive to small adjustments of the optics. It is possible that the long nozzle was even more sensitive to these adjustments, so it conceivable that the more highly collimated beam did not intersect the laser beam.

3.5 Photomultiplier Tube

We use a 51 mm photomultiplier tube (PMT) manufactured by ET Enterprises to detect the fluorescence from atomic transitions. A 670 nm filter with a bandpass of 10 nm is placed over the PMT window to block out ambient light.

The current from the PMT is converted to a voltage by a transimpedance amplifier. Our transimpedance amplifier has a gain of 10^5 V/A and a bandwidth of 20 kHz. We use

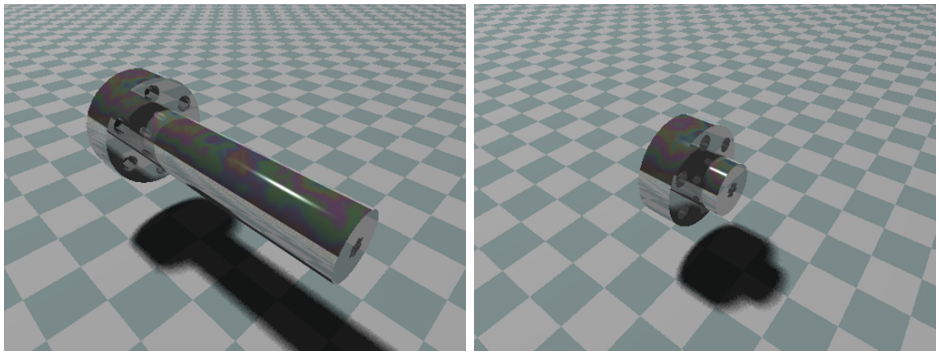

(a) Long Nozzle **(b)** Short Nozzle

Figure 3.21: Renderings of the long (a) and short (b) nozzles. Previously, the long nozzle was used in hopes of producing a more collimated atomic beam. The thought was that a more collimated beam would improve the observed signal sizes, but we encountered significant difficulty in finding resonance signals with the long nozzle. In the current setup, we use the short nozzle. Stainless steel hypodermic needles are inserted in the nozzle channel to produce a collimated beam.

Figure 3.22: Nozzle pictured next to a quarter. The seven stainless steel hypodermic needles can be seen in the central channel.

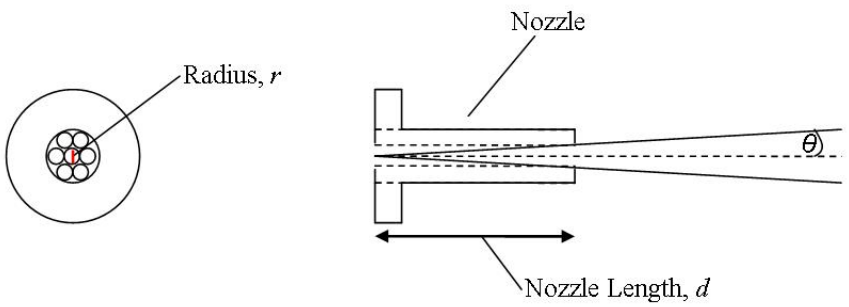

(a) Front view of the nozzle **(b)** Side view of the nozzle

Figure 3.23: Front and side view of the nozzle. In Fig. 3.23a, we see that Seven small circular tubes are inserted in the central channel, each of radius .0595". The small radius of the tubes reduces the Doppler width. In Fig. 3.23b, we see that the angle θ is calculated based on the geometry of the nozzle.

Labview and a 16 bit ADC to digitize and record the PMT signal.

3.6 Doppler Width Estimate

We can obtain an estimate for the size of Doppler broadening by assuming that atoms leaving the oven have an average velocity given by

$$v_{avg} = \sqrt{\frac{8k_BT}{\pi m}} \tag{3.5}$$

and that the angular divergence is given by

$$\theta = \arctan\left(\frac{r/2}{d}\right), \tag{3.6}$$

where r and d are indicated in figure 3.23. Our nozzle design has seven circular tubes inserted into the nozzle channel to further decrease the Doppler width. As mentioned in Sec. 3.4.2, each circular tube has a radius $r = .0595$" and a length $d = .5$".

Since $T \approx 600$ K, the transverse velocity is

$$v_t = v_{avg}\sin(\theta) = \sqrt{\frac{8k_BT}{\pi m}}\frac{r}{d} \approx 80 \text{ m/s}. \tag{3.7}$$

From Eq. 2.81, we obtain as an order of magnitude estimate that $\Delta f \approx 120$ MHz. For comparison, the natural linewidth of the D1 and D2 transitions is ~ 6 MHz, as stated in Sec. 2.7.2.

3.7 Temperature Estimate

As a check for consistency with the temperature we infer from the thermocouple readings, we can estimate the temperature of the atoms based on the measured signal size. A typical fluorescence signal is on the order of 500 mV. The gain of the transimpedance amplifier was 10^5 V/A, while the signal current from the PMT was 5×10^{-6} A. At an operating voltage of 800 V, the gain was about 10^5. The photoelectron current is then the signal current divided by the PMT gain, or roughly 5×10^{-11} A $\approx 3 \times 10^8$ photoelectrons per second. Since the detection efficiency of the PMT is 0.05, the number of photons per second incident on the PMT was about 6×10^9. However, the transmission rate of the interference filter in front of the PMT was only about 0.3 and the detection efficiency was estimated to be roughly 0.05 based on a Monte Carlo calculation, so the number of photons per second scattered was 4×10^{11}. The power of the beam into the chamber was about 50 μW or about 2×10^{14} photons per second. From the beam power and the number of photons per second scattered, we find that the probability of one photon scattering is

$$P_\gamma = \frac{4 \times 10^{11}}{2 \times 10^{14}} = 4 \times 10^{-3} = n\sigma_{abs} z. \tag{3.8}$$

For resonant atoms, the cross section is approximately [27]

$$\sigma_0 = \frac{3\lambda^2}{2\pi} = 2.13 \times 10^{-13} \text{ m}^2. \tag{3.9}$$

Due to the transverse velocity distribution of atoms in the atomic beam, some of the atoms are not resonant with the transition. It is a good estimate that the fraction of resonant

atoms is equal to the ratio of the natural line width to the Doppler line width, so one obtains an effective absorption cross section

$$\sigma_{abs} = \sigma_0 \frac{\Gamma_0}{\Gamma_D} = 1.26 \times 10^{-14} \text{ m}^2. \tag{3.10}$$

Since $P_\gamma = n\sigma_{abs}z$, where $z \approx 1$ cm, one can solve the equation to obtain the beam density

$$n = 10^6 \text{ atoms per cm}^3. \tag{3.11}$$

Since the beam density is a factor of 10^6 times smaller than the oven density (an estimate obtained by comparing the atom density at the nozzle, found from the vapor density curve for Li, to the area over which atoms spread out in the interaction region times the atoms' velocity), the atom density in the oven is about 10^{12} atoms per cm^3. This corresponds to a temperature of 380° C.

This calculated temperature agrees reasonably well with what we measure with our thermocouples. For this particular observed fluorescence peak, the calculation is 10°C lower than the temperature we recorded in the front of the oven and 44°C higher than the temperature recorded in the back of the oven.

3.8 Frequency Standard Stability

In our experiment, the frequency comb is stabilized to a GPS-referenced rubidium atomic clock. Since frequency standards tend to drift over long timescales, a standard deviation calculation is not useful in characterizing the stability of the clock. Instead, a measure called the Allan deviation is more descriptive. The Allan deviation avoids divergence over long timescales by using a series of deviations over sets of neighboring points to determine how the standard deviation changes over time.

3.8.1 Definition of Allan Deviation

If we let $\nu(t)$ be the output frequency of a frequency standard being studied and ν_0 be the frequency of an ideal oscillator, then we can define the normalized frequency deviation as

$$y(t) = \frac{\nu(t) - \nu_0}{\nu_0}. \tag{3.12}$$

The time deviation, $x(t)$, from the initial point $t = 0$ is then the sum of these deviations, or in the continuous case, it is the integral over time of these deviations:

$$x(t) = \int_0^t y(t')dt'. \tag{3.13}$$

The n^{th} average frequency deviation over some interval, τ, is

$$\overline{y}_n = \frac{x_{n+1} - x_n}{\tau}, \tag{3.14}$$

where we have assumed that the spacing τ is small. The "Allan Deviation" is defined as [43]

$$\sigma_y(\tau) = \sqrt{\frac{1}{2}\left\langle(\overline{y}_{n+1} - \overline{y}_n)^2\right\rangle}, \tag{3.15}$$

where the brackets signify an infinite time average. Using Eq. 3.14, the Allan Deviation can be written as

$$\sigma_y(\tau) = \frac{1}{\tau}\sqrt{\frac{1}{2}\left\langle(x_{n+2} - 2x_{n+1} + x_n)^2\right\rangle}. \tag{3.16}$$

The Allan deviation characterizes the stability of an oscillator in terms of the average frequency deviations, $\overline{y}_n$ between neighboring set of points, rather than by deviations of all the points from some average value. Since the Allan deviation is a function of the time interval, τ, over which the average frequency deviation is calculated, it is commonly expressed graphically using a log-log scale.

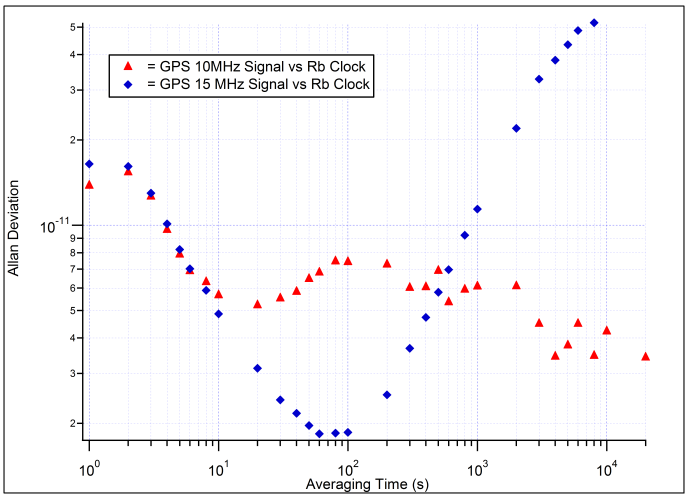

Figure 3.24: The Allan deviation of our rubidium frequency standard compared with various GPS systems, indicated in red and blue. In any time regime, the better of these two curves indicates an upper bound for the accuracy of our frequency standard.

3.8.2 Stability of Our Frequency Standard

In this experiment, our frequency synthesizers use a GPS-referenced rubidium atomic clock as the frequency standard. Figure 3.24 shows that the Allan deviation of our atomic clock is $\sim 10^{-11}$. This translates to an uncertainty in our frequency measurements of about 10 kHz, so at present, the stability of our clock is not a limiting factor in the precision of our measurements.

3.9 Data Collection

Before data collection, the frequency comb must be stabilized and the the frequency of the diode laser must be stabilized to the comb. We stabilize f_{rep} before f_0 because the former is usually more stable. Prior to stabilization of f_b, the angle of the diffraction grating and position of the z-focus in the diode laser cavity are adjusted so that the output power is close to optimal (we typically have about 40μW) and a raw fluorescence signal is observed

on an oscilloscope connected to the PMT. Next, f_{rep} is tuned so that a suitably sized f_b is observed (we aim for a signal to noise ratio of about 40 dB in a 300 kHz bandwidth). Attaining an appropriately sized f_b often involves further adjustments to the alignment of the diode laser and frequency comb. After f_b is optimized, the diode laser is stabilized to the comb. Lastly, the power of the diode laser is observed with a photodiode and actively stabilized by use of an electro-optic modulator (EOM).

The frequency comb is stabilized to an rf signal generator which is controlled by use of Labview. The computer running Labview communicates with the synthesizer via a GPIB connection. When collecting data, a typical scan range for f_{rep} is $\sim$ 1 kHz. In a single scan, the frequency of the rf signal generator is incremented in steps of 1 Hz from the initial to the final frequency, and then it is decreased back to the initial value, giving both an "up" and "down" direction for a single scan. As the frequency is scanned over resonances of the atoms, fluorescence is incident on the PMT and produces a current. The current is converted to a voltage by use of a transimpedance amplifier. This voltage is sent to a 16 bit analog-to-digital converter (ADC). We record $1,000$ samples per channel and $10,000$ samples per frequency point. Labview is used to digitize and record f_{rep}, the PMT signal, the standard deviation of the samples from the PMT signal, the transmission through the Fabry-Perot cavity, the standard deviation of the Fabry-Perot signal, the power of our diode laser, and the standard deviation of the power.

Chapter 4

Results and Analysis

The results of the experiment are presented, interpreted, and discussed in this chapter.

4.1 Density Matrix Calculations of Spectra

The density matrix can be used to gain a better understanding of a number of effects that are present in precision measurement experiments. In this section, we use the density matrix formalism to explore the effects of light polarization and beam power on fluorescence spectra.

4.1.1 Polarization Effects

As noted in Ref. [8, 44], for transitions that are not resolved beyond the homogeneous line width, the polarization angle of the excitation light measured relative to the direction of detection can have a significant effect on the observed lineshapes of atomic spectra. This is the result of a quantum interference effect. When the frequency differences between the different transitions is smaller than the homogeneous line width, the states

are excited coherently. This leads to the interference effects. This polarization effect is particularly dramatic in the ^{7}Li D2 line.

Figure 4.1 shows a density matrix calculation of the ^{7}Li D2 $F = 1 \rightarrow F' = 2, 1, 0$ transitions with fluorescence polarization angles of $0°, 54.7°$ (the magic angle), and $90°$ relative to the direction of detection. As the calculation shows, the different polarization angles both shift the positions and alter the amplitudes of the peaks. For example, there is a relative shift of 1 MHz for the $F = 1 \rightarrow F' = 1$ peak for polarization angles of $0°$ and $90°$. It is also clear that the amplitudes differ depending on the polarization, but it is difficult to isolate the amplitudes because of the interference effects; the amplitudes cannot be assigned to particular $F \rightarrow F'$ transitions.

One can compensate for this effect by ensuring that the detected fluorescence is polarized at the so-called "magic angle." The interference term is proportional to the second order Legendre polynomial, which is

$$P_2(x) = \frac{1}{2}(1 - 3\ \cos^2(\theta)), \tag{4.1}$$

where θ is the angle of detection relative to the excitation. This term is equal to zero when $\theta = 54.7$, the "magic angle" [8, 44].

4.1.2 Saturated Fluorescence

One of the main motivations for saturated fluorescence spectroscopy is that a Doppler-free dip appears at the center frequency of the transition. In principle, this means that the linewidth of the dip is limited only by the natural linewidth of the transition. The dip is the result of a strong pump beam being retroreflected across the atomic beam. Due to the Doppler shifts experienced by atoms moving with transverse velocities, atoms from opposite velocity classes share the excitation demands of the beam. However, for

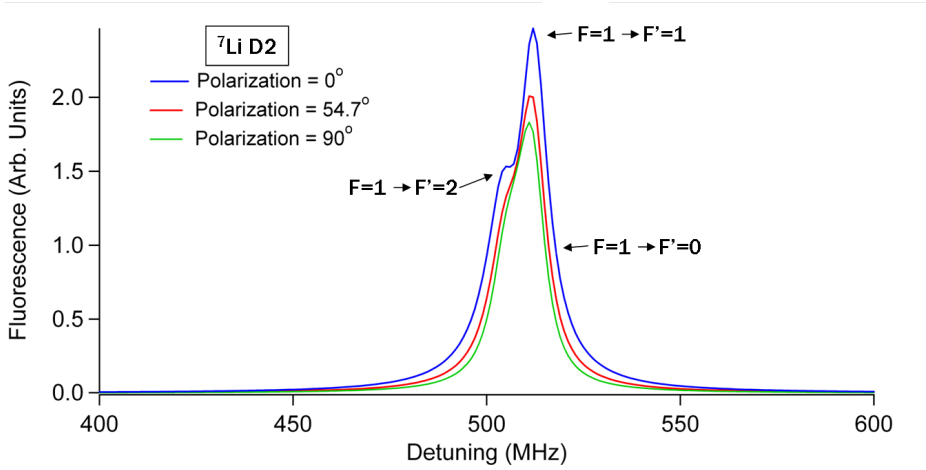

Figure 4.1: Calculated spectra for ^{7}Li D2 $F = 1 \rightarrow F' = 2, 1, 0$ transitions for different polarizations of light relative to the direction of detection. The polarization angles are $0°, 54.7°$ (the magic angle), and $90°$. As seen in the graph, the amplitudes and peak centers are shifted depending on the polarization.

the zero-velocity atoms, the incident beam saturates the transition, resulting in a dip at the center frequency of the transition. The essential components are retroreflection and sufficient power to saturate the transition for the zero-velocity class. Without either one of these, no saturated fluorescence dips will be observed. Figure 4.2 shows a calculation for a two-level system that illustrates the power dependence of the saturated fluorescence dip. As the power of the incident beam is decreased, the dip becomes less prominent and eventually disappears.

A complicating phenomenon in saturated fluorescence spectroscopy as applied to multi-level systems is that extra dips or peaks will sometimes occur. If the fluorescence spectra of transitions sharing an excited or lower energy state overlap within their Doppler width [45], then extra dips, known as crossover resonances, appear. Consider two transitions that overlap within their Doppler width and share a lower level. An incident beam with a frequency halfway between these center frequencies will saturate two velocity classes for the first transition, due to Doppler shifts. However, the reflected beam will saturate one of

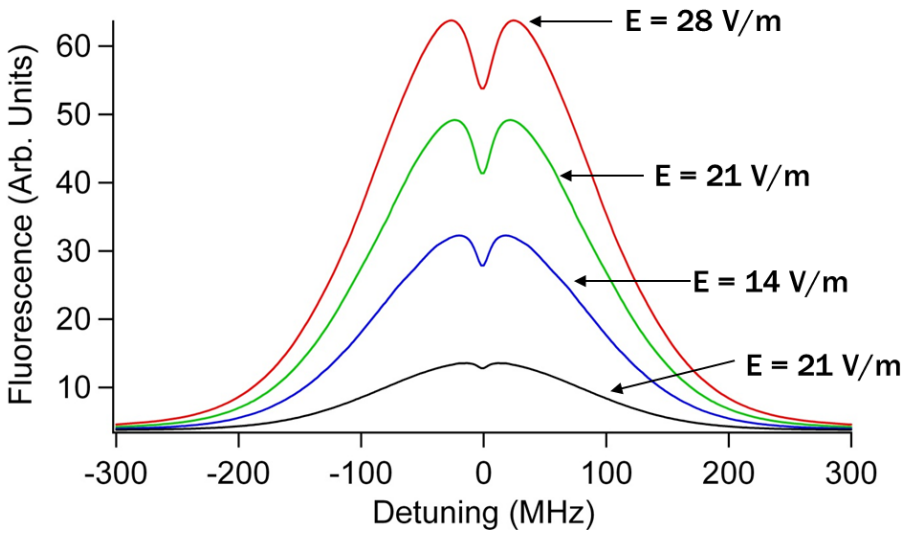

Figure 4.2: Calculated spectra of a two-level system for various strengths of the electric field. As the strength of the electric field is decreased, the saturated fluorescence dip goes away.

the same velocity classes as the incident beam, and this results in a total of three saturated dips, one at each of the transition centers and another halfway in between.

4.2 Data

Raw data from scans over various resonances of ^{7}Li and ^{6}Li are shown in Fig. 4.4. When f_{rep} is scanned, the rf signal generator incremented up to a final frequency and then decremented back to the initial frequency, so each point in frequency is associated with two points in fluorescence signal.

4.2.1 Data Cleaning

After data have been collected, the data sets, or "scans," are loaded into the data analysis program IgorPro. Fluctuations in the various phaselocks make it necessary to discard certain points in data scans, as they add only noise to the measured fluorescence signals. These fluctuations show up as a power variation in the photodiode signal. A

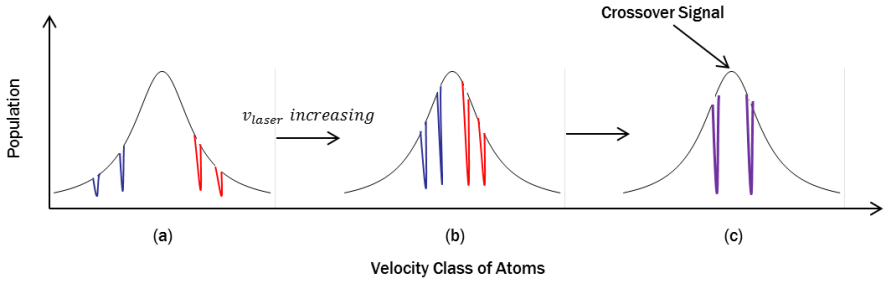

Figure 4.3: A crossover resonance occurs because either the reflected or incident) beam burns a hole in the population distribution that is then excited by the opposite beam on a different transition. In panel (a), the incident (blue) and reflected (red) beams each excite atoms from different velocity classes to two different transitions. In panel (b), the frequency of the laser is tuned, and the excited velocity classes move towards each other, since one of the beams is retroreflected. Finally, in panel (c), the incident beam saturates one of the transitions for a velocity class, but the reflected beam saturates the same velocity class for the other transition, leading to a crossover resonance.

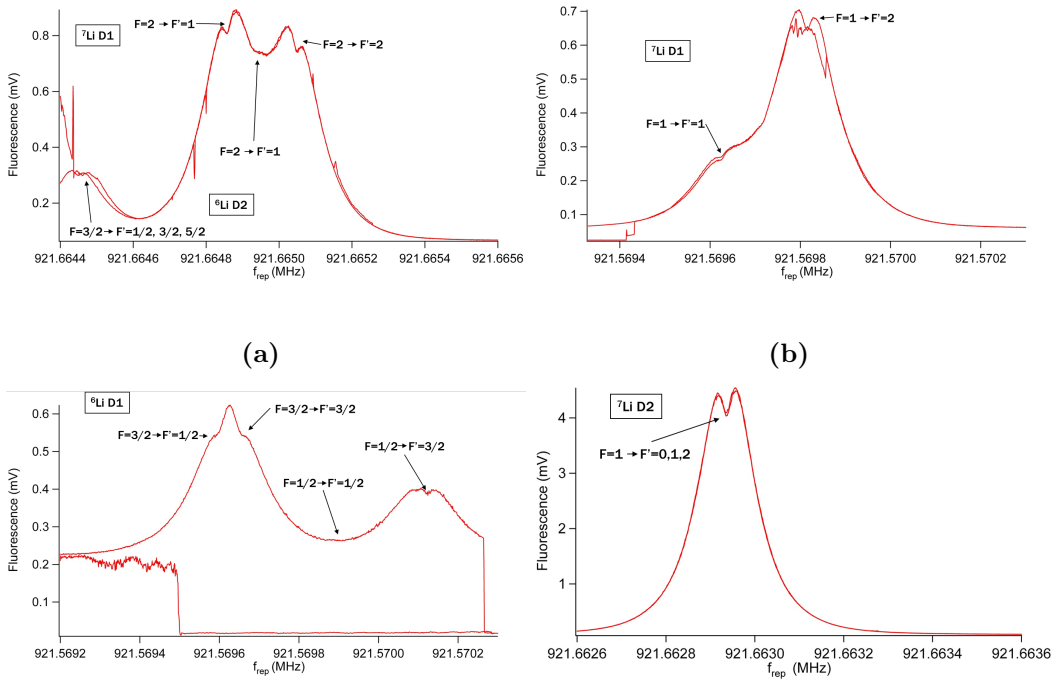

Figure 4.4: Raw data collected for this experiment.

procedure is run that checks whether each point in the laser power data set is within a particular range. For example, the procedure will check whether the power associated with a particular point is within three standard deviations of the average power. If the power lies within this range, then the the data associated with this point remain unchanged. If the power is more than three standard deviations from the average power, then all data (meaning the values for f_{rep}, the PMT signal, the standard deviation of the samples from the PMT signal, the transmission through the Fabry-Perot cavity, the standard deviation of the Fabry-Perot signal, the power of our diode laser, and the standard deviation of the power signal) for this point are discarded. This cleaning procedure is repeated multiple times to eliminate noise from the raw data.

Even after this initial cleaning phase, a visual inspection of the PMT signal vs. f_{rep} plots will often reveal that noisy portions of the data remain. These values are removed by hand.

4.2.2 Converting f_{rep} to an Absolute Frequency and Peak Identification

From Eq. 3.1, we know that f_{rep} can be converted into an absolute frequency if one knows the mode number, n, the repetition rate, f_{rep}, and the effective offset. In this case, the effective offset is given by the sum of the offset frequency, f_0, and the beat frequency, f_b. However, as mentioned in Secs. 3.1.5 and 3.2.3, it is not clear whether the signs of f_0 and f_b are positive or negative. Without knowledge of their signs, one is left

with four possibilities for converting f_{rep} into an absolute frequency:

$$\begin{aligned} \nu_1 &= nf_{rep} + f_0 + f_b, \\ \nu_2 &= nf_{rep} + f_0 - f_b, \\ \nu_3 &= nf_{rep} - f_0 + f_b, \\ \nu_4 &= nf_{rep} - f_0 - f_b. \end{aligned} \tag{4.2}$$

By comparing the experimental spectra to spectra with identified peaks, and by using other clues such as the relative detunings of peaks, one can unambiguously determine which transitions the peaks correspond to, and thus the absolute transition frequencies belonging to those peaks. This initial guess is tested by solving Eqs. 4.2 for n for given f_{rep}, f_0, and f_b. Since n has to be an integer, it is likely that only one equation will yield a value for n that is close to an integer. After this prescription is used to determine n, the measured frequencies can be converted into absolute frequencies using Eq. 3.1.

4.2.3 Cleaned Data with Identified Peaks

A number of the observed spectra with identified peaks are shown in Fig. 4.5. These data have been cleaned according to the procedure outlined in Sec. 4.2.1 The data show a number of transitions from the ^{7}Li D1, D2 and ^{6}Li D1, D2 transitions.

In Fig. 4.6, we see the ^{7}Li D2 $F = 1 \rightarrow F' = 1$ transition scanned over multiple times at different powers of the diode laser (the $F' = 0, 2$ transitions are also present, but unresolved). This clearly shows how the saturation dip disappears as the beam power is decreased. These actual data agree qualitatively with the two-level model spectra, pictured in Fig. 4.2, showing the same phenomenon.

Finally, in Fig. 4.7, we see the ^{7}Li D1 and ^{6} Li D2 transitions for both a retroreflected and a non-retroreflected beam. As we expect, the non-retro beam shows no saturated fluorescence dip.

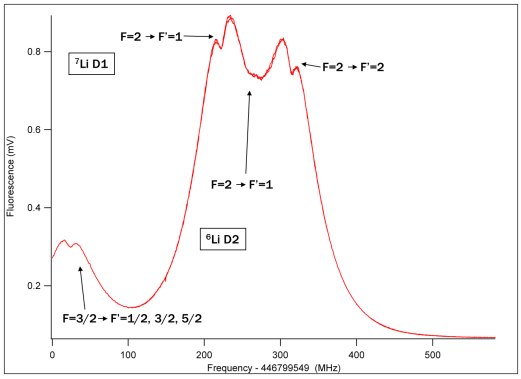

(a) Cleaned data for the ^{6}Li D1 $F = 2 \rightarrow F' = 1, 2$ and ^{6}Li D2 $F = 3/2 \rightarrow 1/2, 3/2, 5/2$ transitions.

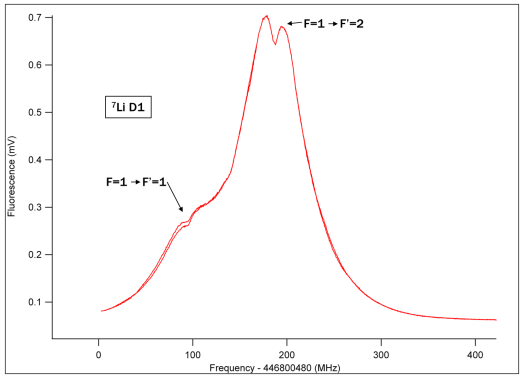

(b) Cleaned data for the ^{7}Li D1 $F = 1 \rightarrow F' = 1, 2$ transitions.

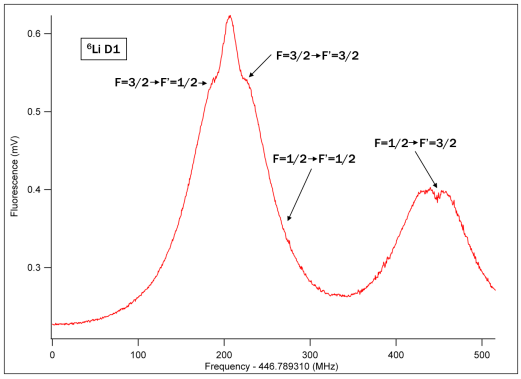

(c) Cleaned data for the ^{6}Li D1 $F = 3/2 \rightarrow 1/2, 3/2$ transitions.

Figure 4.5: Cleaned data showing the fluorescence spectra for various transitions in ^{7}Li and ^{6}Li.

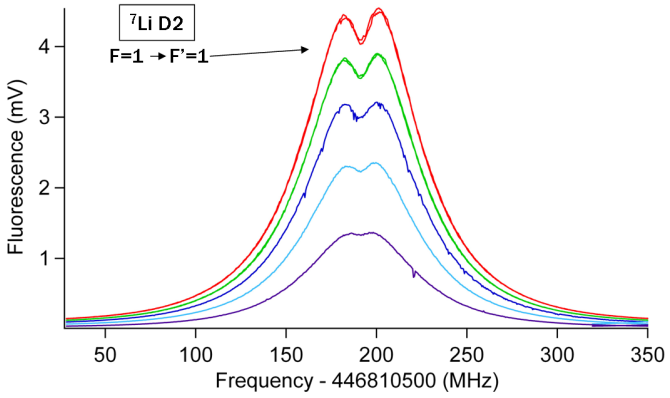

Figure 4.6: These data are all of the same isolated peak of the ^{7}Li D2 $F = 1 \rightarrow F' = 1$ transition, but for various levels of power. The frequency comb and diode laser happened to remain stable during this scan. The resonance was scanned over continuously and the power was reduced at the end of each loop. The saturated fluorescence dip becomes less prominent and eventually disappears as the power is decreased, in agreement with the model in Sec. 4.1.2.

4.3 Curve Fitting

To extract the saturated fluorescence locations from the data, the sections of the data containing the dips were removed and the remaining data were fit. The fit was then subtracted from the experimental spectra, leaving the saturated fluorescence peaks. Since the lineshape for atomic fluorescence spectra is neither Gaussian nor Lorentzian, the data were fit using a number of different functions, each consisting of of a Gaussian, a Lorentzian, and an additional term to account for the observed asymmetry, all multiplied together. Through trial and error, the following fit function was arrived at:

$$F_(\nu) = B + \sum_i A_i e^{\frac{-(\nu-\nu_i)^2}{2\sigma^2}} \frac{\frac{\gamma^2}{4}}{\frac{\gamma^2}{4} + (\nu-\nu_i)^2} \left(1 + \sum_{n=1}^{10} c_n(\nu-\nu_i)^n\right), \tag{4.3}$$

where the sum is taken over the number of resonance peaks present. The fit has one baseline offset term (B), i peak amplitude terms (A_n), i terms defining the center of the peaks (ν_i), two terms describing the widths of the Gaussian and Lorentzian curves (γ and σ), and finally 10 coefficients (c_i) for the tenth-degree polynomial. This gives a total of $2i + 13$

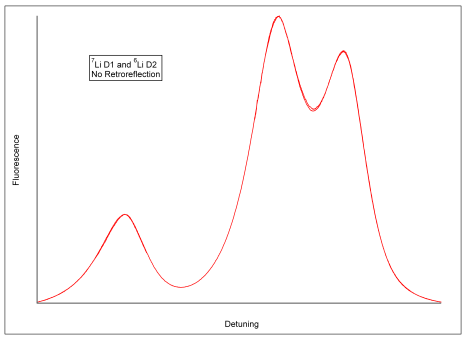

(a) No retroreflection

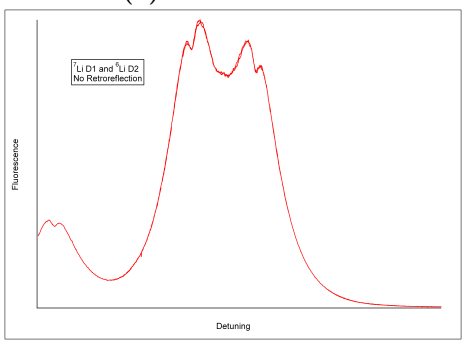

(b) Retroreflection

Figure 4.7: Figures 4.7a and 4.7b show scans of ^{7}Li D1 and ^{6} Li D2 resonances that were performed while the retroreflected beam was blocked and unblocked, respectively. In the blocked case, there are no saturated fluorescence dips present. On the other hand, when the beam was unblocked, dips were present.

free parameters for each fit, where i is the number of peaks. The fits were weighted by the standard deviation of the PMT voltage divided by $\sqrt{N}$, where $N = 10^4$, the number of samples per frequency point. These fits are shown in Fig. 4.8, along with calculations of the lineshapes and associated saturated fluorescence spectra. The modeled spectra were obtained through a density matrix calculation. See appendix 2 for the code used to produce these plots.

The χ^2 values for the fits shown in Figs. (a), (b), and (c) were 9.3×10^4 (1488 points), 5.4×10^4 (547 points), and 2.7×10^4 (789 points), respectively. The large χ^2 values could be an indicator that we are oversampling and consequently that the estimate of the uncertainty is too small due to the correlation of the samples.

The fits were especially sensitive to the coefficients for higher order terms in the polynomial factor, so the fits were produced iteratively. They were first computed by fixing all of the c_i coefficients to be zero. For the preliminary fits, the relative differences between the peak positions were also fixed based on the values given in [8]. The resulting values were then substituted as the initial values for the fit and fixed parameters were gradually freed.

The structure of the residuals in (b) are almost absent. However, the residuals shown in Figs. (a) and (c) show that there are some problems with the fit for ^{7}Li D1 $F = 2 \rightarrow F'$, ^{6}Li D2 $F = 3/2 \rightarrow F'$, and ^{6}Li D1 $F = 3/2 \rightarrow F'$ transitions. The residuals for (c) show significant fluctuations where the data were removed. The failure of this fit can be seen in (f), as the data near 200 MHz rise above the fit. In plot (e), we can see that the fit diverges from the data when compared on the right part of the graph. Moving to the middle, to the saturated fluorescence dip, we can see that the fit is displaced slightly to the left of the data throughout the entire region that was removed for the fit. Despite the appearance of the residuals, there is still an asymmetry to the peak that is not entirely

described by the fit we have chosen.

Two crossover resonances are evident in these data. The crossover peak in (h) is particularly clear. As expected, it lies halfway between the $F = 1 \rightarrow F' = 1$ and $F = 1 \rightarrow F' = 2$ peaks. Additionally, since the resonance occurs halfway between two transitions sharing a lower state (^{7}Li D1 $F = 1$), we would expect a dip in the data, and therefore a peak when the fit is subtracted off. However, the relative amplitude does not match up perfectly with the calculation shown in (k). There is also a noticeable crossover dip in plot (i). This is corroborated by the calculation in plot (l), which shows similar relative amplitudes for the corresponding peaks in plot (i).

Three peaks in (g) are clearly resolved, namely the ^{6}Li D2 $F = 3/2 \rightarrow F'$, and ^{7}Li D1 $F = 2 \rightarrow F' = 1, 2$ transitions. However, the spectra calculation in plot (j) reveals that the ^{6}Li $F = 2 \rightarrow F' = 1$ peak is also present in this region. However, its amplitude is small relative to the peaks surrounding it. Additionally, the calculation indicates that there is a cross over resonance between the ^{7}Li D1 $F = 2 \rightarrow F' = 1, 2$ peaks, as we would expect since their separation is on the order of the natural linewidth of lithium. This further complicates the resolution of the ^{6}Li $F = 2 \rightarrow F' = 1$ transition and suggests that saturated fluorescence spectroscopy might not be suitable for resolving peaks located between other peaks whose separation is on the order of the natural linewidth of lithium.

4.4 Systematics

Zeeman splitting and ac Stark shifts are systematic effects that play an important role in this experiment. Zeeman splitting arises because of the earth's magnetic field. To compensate, we have constructed three sets of orthogonal coils in a near Helmholtz coil configuration around the vacuum chamber and zeroed the magnetic field at the interaction

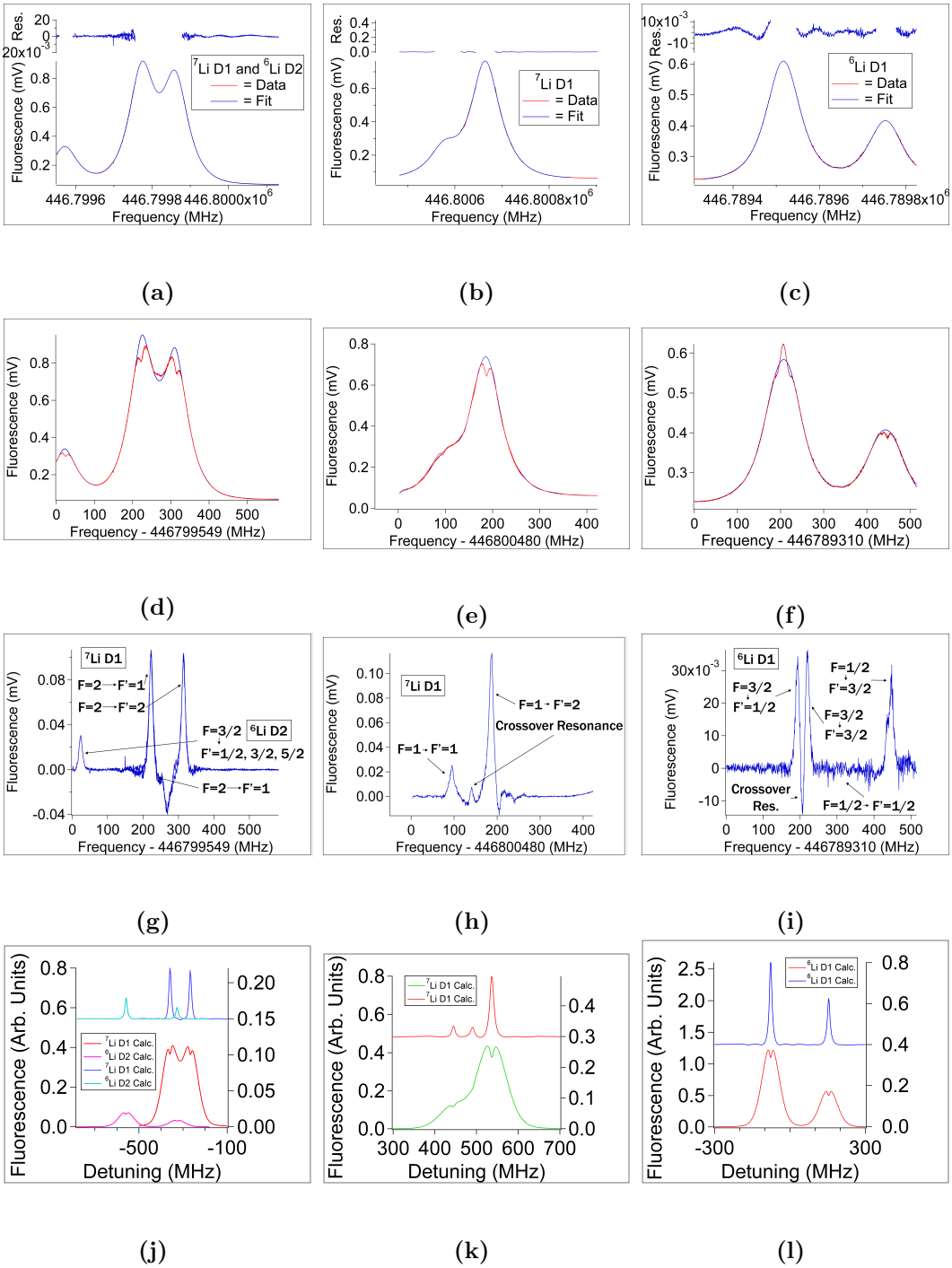

Figure 4.8: To gain a higher resolution of peak centers, the portions of the spectra containing the saturated fluorescence dips were removed, and the data remaining were fit. Each original dataset was then subtracted from its corresponding fit. This is summarized moving from the top row to the third row. The last row contains modeled spectra, which were generated through a density matrix calculation.

region. Assuming that the we have zeroed the magnetic field to within 10 mG, we can make a rough estimate of the size energy splitting in the $^2P_{1/2}$ state of ^{7}Li, which has $g_J \approx 2/3$. Using Eq. 2.5.8, we have

$$\Delta E = \mu_B g_J M_J B \approx 9.4 \times 10^3 \text{ Hz}. \tag{4.4}$$

This corresponds to a frequency shift of about 10 kHz. Since this is less than the natural linewidth of lithium, the result is a slight broadening of the lineshape. This systematic effect can be eliminated by intentionally splitting the lines through application of a strong magnetic field, which would be done using the coils. Since the splitting scales linearly with the strength of the magnetic field, the splitting can be plotted vs. the magnetic field, and then extrapolated to zero.

Another important systematic effect is the ac Stark shift. The ac Stark shifts in this experiment are a caused by the laser that excites the transitions. We can use Eq. 2.70 to estimate the ac Stark shifts for the ^{7}Li D1 $F = 1 \rightarrow F' = 1$ transition. Assuming a beam radius of 1 mm and a power of 40 μW, and noting that the intensity is proportional to the square of the electric field, we obtain an an electric field of $\sim$ .8 V/cm. Using the separation between the resonance, $\omega - \omega_0 \approx 2\pi \times (10$ MHz), the approximation $d \approx 1.28$ MHz/(V/cm), and using the estimate that the electric field from the laser is $\varepsilon \approx .8$ V/cm, we have

$$\Delta E \approx \frac{d^2\varepsilon^2}{4\hbar(\omega - \omega_0)} \approx 1.2 \times 10^4 \text{ Hz}, \tag{4.5}$$

which converts to a frequency shift of $\sim$ 80 MHz. Since ac Stark shifts are proportional to the square of electric field, the shift could be plotted against power and extrapolated to zero, which would eliminate this systematic uncertainty.

The uncertainty of our frequency standard also contributes to the uncertainty budget, but is not currently a limiting factor. Our frequency standard is accurate to roughly

2 parts in 10^{-11} [37]. The uncertainty in our frequencies is then

$$\delta\nu = \sqrt{\delta f_b^2 + \delta f_0^2 + n\delta f_{rep}^2}, \tag{4.6}$$

and since n is on the order of 4×10^5, the uncertainty contributions from f_b and f_0 are negligible, and we obtain

$$\begin{aligned} \delta\nu \approx n\delta f_{rep} &= 2 \times 10^{11} \times 4 \times 10^5 \times 1 \text{ GHz} \\ &\approx 10 \text{ kHz}. \end{aligned} \tag{4.7}$$

This is comparable to the uncertainty from Zeeman splitting.

The statistical uncertainty of our current measurements offers a small contribution to the uncertainty. The maximum shot noise for which a peak can be resolved is given by

$$\delta\nu = \frac{\gamma}{\sqrt{N}}, \tag{4.8}$$

where γ is the width of the peak and N is the number of scattered photons. With $\gamma \approx$ 80 MHz and $N \approx 10^{11}$, $\delta\nu \approx 250$ Hz.

The fit uncertainties are currently the most significant limiting factor in the accuracy of our measurements. Since saturated fluorescence spectroscopy results in Doppler-free dips, we would expect the subtracted off data (Fig. 4.8 (g), (h), and (i)) to be described by Lorentzian curves, bu this is not the case. The relatively poor quality of the subtracted off data may limit the experiment using the saturated fluorescence technique.

Chapter 5

Conclusions

We have presented preliminary data from an experiment aimed at high-precision measurement of Li D1 and D2 lines. For transitions whose relative separation is on the order of the natural linewidth, the inevitable emergence of crossover signals adds an additional layer of complexity to saturated fluorescence spectra. When a saturated fluorescence dip occurs near a transition peak, it becomes difficult to resolve the location of the transition. Addressing this issue will likely involve further investigation of the power dependence of saturated fluorescence lineshapes, and may ultimately mean that saturated fluorescence spectroscopy is not suitable for resolution of transitions whose separation is comparable to the natural linewidth.

Regardless of whether saturated fluorescence continues to be used in this experiment, extracting meaningful precision measurements will mandate a careful consideration of the uncertainty budget. In principle, statistical uncertainty is only limited by the accuracy of our frequency standard, which is about 2 parts in 10^{-11} [37]. When the various locks remain stable, the signal to noise ratio of our data is also very high, as indicated by the smoothness of the observed spectra.

The poor quality of the curve fitting, as indicated by the subtracted-off fits shown in Figs. 4.8 (g), (h) and (i), is a severely limiting factor. There is an inherent asymmetry in the data, and it is not clear what sort of fit should be used. Ideally, the Doppler-free transitions in the subtracted-off fit should have Lorentzian profiles, but this is clearly not what we observed. In addition to the noisy quality of these fits, there are sometimes crossover resonances that further obscure the underlying lineshape of the transitions. Proper curve fitting must be further investigated, and it may ultimately indicate that an approach besides saturated fluorescence spectroscopy will be necessary.

5.1 Future Directions

In the future, we intend to implement a magneto-optical trap (MOT) to eliminate the Doppler width. The MOT cools and traps atoms using a number of lasers and an inhomogeneous magnetic quadrupole field. The inhomogeneous field is produced by current flowing in opposite directions through magnetic coils in an anti-Helmholtz configuration. Atoms at the center of the MOT are exposed to laser light from 6 axial directions. For atoms at the center of the trap, the magnetic field is zero, and the total momentum absorbed is zero because the absorption rates are equal for the 6 incident laser beams. Atoms that are not at the center will have their magnetic sublevels split. Consequently, they experience a net transfer of momentum which forces them back to the center of the trap, so there is a restoring force for atoms not at the center. For a more detailed discussion of Doppler-cooling and MOTs, see Refs. [45, 46]. Figure 5.1 shows an example setup for a MOT.

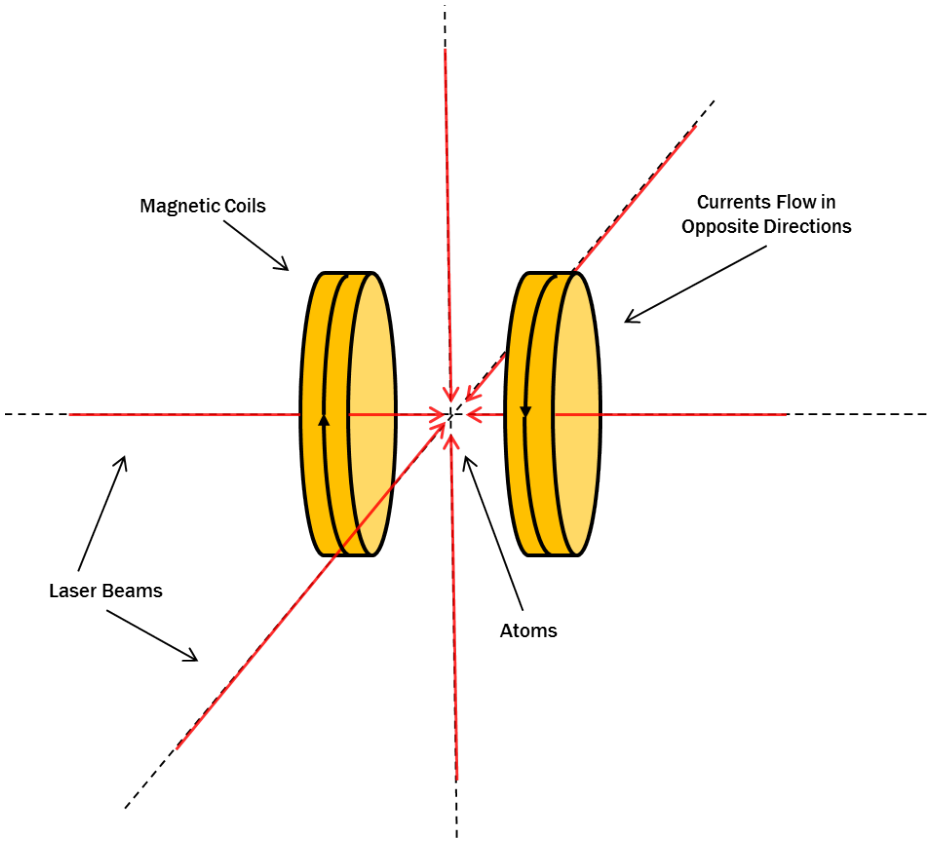

Figure 5.1: Sample setup for a magneto-optical trap. The separation between the coils is equal to the radius. Current flows in opposite directions through the coils, producing an inhomogeneous magnetic field at the center of the the MOT. Atoms are exposed to laser light from six directions. Atoms offset from the center of the trap have their magnetic sublevels split and experience a restoring force towards the center. Atoms at the center experience no magnetic field and experience a net force of zero.

Bibliography

[1] Z.-C. Yan and G. W. F. Drake. *Phys. Rev. A*, 52:3711, 1995.

[2] Z.-C. Yan, M. Tambasco, and G. W. F. Drake. *Phys. Rev. A*, 57:1652, 1998.

[3] X.-X. Guan and Z. W. Wang. *Eur. Phys. J. D*, 2:21, 1998.

[4] Z.-C. Yan and G. W. F. Drake. *Phys. Rev. A*, 61:022504, 2000.

[5] K. Pachuki. *Phys. Rev. A*, 66:062501, 2002.

[6] M. Puchalski, A. M. Moro, and K. Pachucki. *Phys. Rev. Lett.*, 97:133001, 2006.

[7] F. W. King. *Advances in Atomic, Molecular, and Optical Physics*, 40:57, Academic Press 1999.

[8] C. J. Sansonetti, C. E. Simien, J. D. Gillaspy, J. N. Tan, S. M. Brewer, R. C. Brown, S. Wu, and J. V. Porto. *Phys. Rev. Lett.*, 107:023001, 2011.

[9] H. Orth, H. Ackerman, and E. W. Otten. *Z. Phys. A*, 273:221, 1975.

[10] C. J. Sansonetti et al. *Phys. Rev. A*, 52:2682, 1995.

[11] W. Scherf et al. *Z. Phys. D*, 36:31, 1996.

[12] G. A. Noble et. al. *Phys. Rev. A*, 74:012502, 2006.

[13] D. Das and V. Natarajan. *Phys. Rev. A*, 75:023001, 2007.

[14] Z.-C. Yan, W. Nörterhäuser, and G. W. F. Drake. *Phys. Rev. Lett.*, 100:243002, 2008.

[15] Z.-C. Yan and G. W. F. Drake. *Phys. Rev. A*, 66:042504, 2002.

[16] M. Puchalski and K. Pachucki. *Phys. Rev. A*, 79:032510, 2009.

[17] B. H. Bransden and C. J. Joachain. *Physics of Atoms and Molecules*. Longman, 1983.

[18] J. R. Delaeter, J. K. Böhlke, P. DeBiévre, H. Hidaka, H. S. Peiser, K. J. R. Rosman, and P. D. P. Taylor. *Pure Appl. Chem.*, 75:683, 2003.

[19] D. J. Griffiths. *Introduction to Quantum Mechanics*. Prentice Hall, 1995.

[20] G. Herzberg. *Atomic Spectra and Atomic Structure*. Dover, Second edition, 1944.

[21] L. J. Radziemski, R. Engleman, and J. W. Brault. *Phys. Rev. A*, 52:4462, 1995.

[22] C. J. Lorenzen and K. Niemax. *Phys. Scrip.*, 27:300, 1983.

[23] B. A. Bushaw, W. Nortershauser, G. Ewald, A. Dax, and G. W. F. Drake. *Phys. Rev. Lett.*, 91:043004, 2003.

[24] D. Halliday, R. Resnick, and J. Walker. *Fundamentals of Physics*. Wiley, Seventh edition, 2005.

[25] K. Beloy and A. Derevianko. *Phys. Rev. A*, 78:032519, 2008.

[26] A. Corney. *Atomic and Laser Spectroscopy*. Oxford University Press, Second edition, 1977.

[27] D. Budker, D. F. Kimball, and D. P. DeMille. *Atomic Physics: An Exploration through Problems and Solutions*. Oxford University Press, 2004.

[28] B. Odom, D. Hanneke, B. D'Urso, and G. Gabrielse. *Phys. Rev. Lett.*, 97:030801, 2006.

[29] J. Baron. Precision Spectroscopy of Atomic Lithium With an Optical Frequency Comb. Honors Thesis, Oberlin College, 2012.

[30] I. I. Sobelman. *Atomic Spectra and Radiative Transitions*. Springer, Second edition, 1992.

[31] J. J. Sakurai. *Modern Quantum Mechanics*. Addison-Wesley, 1985.

[32] M. Auzinsh, D. Budker, and S. M. Rochester. *Optically Polarized Atoms: Understanding Light-Atom Interactions*. Oxford University Press, 2010.

[33] S. T. Cundiff and J. Ye. *Rev. of Modern Physics*, 75:325, 2003.

[34] A. Bartels. *Femtosecond Optical Frequency Comb: Principle, Operation and Applications*. Springer, 2005.

[35] S. B. Bernfeld. Stabilization of a Femtosecond Laser Frequency Comb. Honors Thesis, Oberlin College, 2009.

[36] J. K. Ranka, R. S. Windeler, and A. J. Stenz. *Opt. Lett.*, 25:25, 2000.

[37] S. L. Chen. Two-Photon Direct Frequency Comb Spectroscopy of Rubidium. Honors Thesis, Oberlin College, 2012.

[38] K. C. Harvey and C. J. Myatt. *Optics Letters*, 16:910, 1991.

[39] M. G. Boshier, D. Berkeland, E. A. Hinds, and V. Sandoghdar. *Opt. Comm.*, 85:355, 1991.

[40] F. L. Pedrotti and L. S. Pedrotti. *Introduction to Optics*. Prentice-Hall, 1987.

[41] R. W. Boyd. *Nonlinear Optics*. Academic Press, 3rd edition.

[42] W. M. Haynes, editor. *Handbook of Chemistry and Physics*. The Chemical Rubber Company, 92nd edition, 2011-2012.

[43] D. B. Sullivan, D. W. Allan, D. A. Howe, F. L. Walls, editors. *Characterization of Clocks and Oscillators*. U.S. Government Printing Office, 1990.

[44] R. Walkup, A. L. Migdall, and D. E. Pritchard. *Phys. Rev. A*, 25:3114, 1981.

[45] W. Demtröder. *Laser Spectroscopy: Basic Concepts and Instrumentation*. Springer, 3rd edition.

[46] H. J. Metcalf and P. Straten. *Laser Cooling and Trapping*. Springer, 1999.

Appendix A

Two-Level Density Matrix Calculation

The following is a two-level density matrix calculation implemented in Mathematica, authored by J. E. Stalnaker. The Atomic Density Matrix (ADM) package found at http://budker.berkeley.edu/ADM/ was used in this calculation. This package was developed by D. Budker and S. Rochester. The ADM package was accessed on Jan. 28, 2013. This code was used to produce Fig. 2.5.

Density Matrix Calculation for Two-Level Atom with Saturated Fluorescence Spectroscopy

Load Atomic Density Matrix Package

```
<< AtomicDensityMatrix`

(*ParallelEvaluate[<<AtomicDensityMatrix`];*)

values = {
   α → 7500,
   ω0 → 446 789 596.091, (*Center of Gravity for D1 Transition in MHz*)
   Γ → 6, (*Natrual Linewidth in MHz*)
   ΩR → 10, (*Rabi Frequnecy in MHz*)
   γT → 0.1, (*Transit Linewidth in MHz*)
   k → 1/(671. × 10^-7) 1/10^6, (*k in units of 1/(2 π cm)*)
   (*e→1,
   ReducedME[1,{Dipole,1},2]→1,*)
   BranchingRatio[2, 1] → 1 (*Branching Ratio for Decay *)
  };
```

Define Atomic System

Ground State is labeled "1" and Excited State is labeled "2"

```
sys = {
   AtomicState[1],
   AtomicState[2]
  };
```

Display Density Matrix

```
DensityMatrix[sys] // MatrixForm
```

$$\begin{pmatrix} \rho_{1,1}[t] & \rho_{1,2}[t] \\ \rho_{2,1}[t] & \rho_{2,2}[t] \end{pmatrix}$$

Define Optical Field

```
optf = OpticalField[ω + k v + ϕ, E0, {0, 0}] +
  OpticalField[ω - k v - ϕ, E0, {0, 0}](*x-polarized light*)
```

$$\left\{e^{-i\,t\,(-k\,v-\phi+\omega)}\,E0 + e^{-i\,t\,(k\,v+\phi+\omega)}\,E0,\ 0,\ 0\right\}$$

Define Hamiltonian

```
(Simplify[h =
     Hamiltonian[sys, ElectricField → (optf /. E0 → ΩR / ReducedME[1, {Dipole, 1}, 2])]] /.
   {Energy[1] → 0, Energy[2] → ω0}) // MatrixForm
```

$$\begin{pmatrix} 0 & -\Omega R\,(\mathrm{Cos}[t\,(k\,v+\phi-\omega)] + \mathrm{Cos}[t\,(k\,v+\phi+\omega)]) \\ -\Omega R\,(\mathrm{Cos}[t\,(k\,v+\phi-\omega)] + \mathrm{Cos}[t\,(k\,v+\phi+\omega)]) & \omega 0 \end{pmatrix}$$

Unitary Matrix for Rotating Wave Approximation

```
(uRWA = MatrixExp[𝑖 t DiagonalMatrix[Table[If[i ≤ 1, 0, ω], {i, 1, 2}]]]) // MatrixForm
```

$$\begin{pmatrix} 1 & 0 \\ 0 & e^{i t \omega} \end{pmatrix}$$

Hamiltonian in the Rotating Frame

Transformed Hamiltonian before RWA

```
(hRWA = FullSimplify[uRWA.h.Inverse[uRWA] + 𝑖 D[uRWA, t].Inverse[uRWA]] /. {ω → ω0 + Δ} //
    TrigToExp) // MatrixForm
```

$$\begin{pmatrix} \text{Energy}[1] & -\frac{1}{2} e^{-i t (k v+\phi)} \Omega R - \frac{1}{2} e^{i t (k v+\phi)} \Omega R - \frac{1}{2} e^{-i t (k v+\phi)-2 i t (\Delta+\omega 0} \\ -\frac{1}{2}\left(e^{-i t (k v+\phi)} + e^{i t (k v+\phi)}\right)\left(1 + e^{2 i t (\Delta+\omega 0)}\right)\Omega R & -\Delta - \omega 0 + \text{Energy}[2] \end{pmatrix}$$

```
(hPrime = hRWA /. {e^(2 𝑖 t (Δ+ω0)) → 0, e^(-2 𝑖 t (Δ+ω0)) → 0,
      e^(-𝑖 t (k v+ϕ)-2 𝑖 t (Δ+ω0)) → 0, e^(𝑖 t (k v+ϕ)-2 𝑖 t (Δ+ω0)) → 0}) // MatrixForm // Simplify
```

$$\begin{pmatrix} \text{Energy}[1] & -\frac{1}{2} e^{-i t (k v+\phi)}\left(1 + e^{2 i t (k v+\phi)}\right)\Omega R \\ -\frac{1}{2}\left(e^{-i t (k v+\phi)} + e^{i t (k v+\phi)}\right)\Omega R & -\Delta - \omega 0 + \text{Energy}[2] \end{pmatrix}$$

Transformed Hamilitonian after the RWA

```
(*(hPrime=Simplify[hRWA/.(Exp[ExpandAll[a_.ω t+c_.]]→0)//.
      {ω→(ω1+ω2)/2, ω1→(ω0+Δ1), ω2→(ω0+Δ2)}])//MatrixForm*)
```

Relaxation Hamiltonian

```
MatrixForm[
 relax = (IntrinsicRelaxation[sys] /. {NaturalWidth[1] → 0, NaturalWidth[2] → Γ}) +
   TransitRelaxation[sys, γT]]
```

$$\begin{pmatrix} \gamma T & 0 \\ 0 & \Gamma + \gamma T \end{pmatrix}$$

Repopulation Hamiltonian

```
repop = ( γT + Γ   0
            0     γT );
```

Equations of Motion

```
TableForm[eqs = Flatten@LiouvilleEquation[sys, hPrime, relax, repop] //.
    {Energy[1] → 1, Energy[2] → ω0, ϕ → 0} //. values]
```

$$\rho_{1,1}'[t] = 6.1 - 0.1\,\rho_{1,1}[t] - i\left(5\left(e^{(0.-0.0149031\,i)\,t\,v} + e^{(0.+0.0149031\,i)\,t\,v}\right)\rho_{1,2}[t] + \left(-5\,e^{(0.-0.0149031\,i)\,t\,v}\right.\right.$$
$$\rho_{1,2}'[t] = -3.1\,\rho_{1,2}[t] - i\left(-\left(-5\,e^{(0.-0.0149031\,i)\,t\,v} - 5\,e^{(0.+0.0149031\,i)\,t\,v}\right)\rho_{1,1}[t] + \rho_{1,2}[t] + \Delta\,\rho_{1,2}[t] + \right.$$
$$\rho_{2,1}'[t] = -3.1\,\rho_{2,1}[t] - i\left(-5\left(e^{(0.-0.0149031\,i)\,t\,v} + e^{(0.+0.0149031\,i)\,t\,v}\right)\rho_{1,1}[t] - \rho_{2,1}[t] - \Delta\,\rho_{2,1}[t] + 5\,(e\right.$$
$$\rho_{2,2}'[t] = 0.1 - i\left(-5\left(e^{(0.-0.0149031\,i)\,t\,v} + e^{(0.+0.0149031\,i)\,t\,v}\right)\rho_{1,2}[t] - \left(-5\,e^{(0.-0.0149031\,i)\,t\,v} - 5\,e^{(0.+0.01\right.$$

```
TableForm[inits =
  Flatten@InitialConditions[sys, Table[If[i ≤ 1 && i == j, 1, 0], {i, 1, 2}, {j, 1, 2}], 0]]
```

$$\rho_{1,1}[0] = 1$$
$$\rho_{1,2}[0] = 0$$
$$\rho_{2,1}[0] = 0$$
$$\rho_{2,2}[0] = 0$$

```
startFreq = -300;
stopFreq = 300;
δf = 2;
startV = 0;
stopV = 20 000;
δV = 50;
freqSteps = (stopFreq - startFreq)/δf + 1;
vSteps = (stopV - startV)/δV + 1;
pVel = {};
AbsoluteTiming[
 Do[{
    p = Table[DensityMatrix[sys] //.
       NDSolve[{eqs /. values /. v → vi /. ϕ → 0, inits}, DMVariables[sys], {t, 0, 1.5},
         AccuracyGoal → 3, PrecisionGoal → 3][[1]], {Δ, startFreq, stopFreq, δf}];
    pV0MFn[t_] = p;
    pVel = Append[pVel, Table[{startFreq + (j - 1) δf,
        Mean[Table[pV0MFn[t][[j]], {t, 0, 1.5, 0.1}]]}, {j, 1, freqSteps}]];
    Print[vi];
   }, {vi, startV, stopV, δV}];]

dopDist[v_] := e^(-v^2/α^2) /. α → 7500

vIntSpec =
  Table[
   {Take[pVel, {1}][[1]][[i]][[1]],
    Sum[dopDist[startV + δV (j - 1)] Chop[Take[pVel, {j}][[1]][[i]][[2]][[2]][[2]],
      {j, 1, vSteps}] + Sum[dopDist[startV + δV (j - 1)]
       Chop[Take[pVel, {j}][[1]][[i]][[2]][[2]][[2]], {j, 2, vSteps}]},
   {i, 1, freqSteps}];
ListPlot[vIntSpec, PlotRange → All]
```

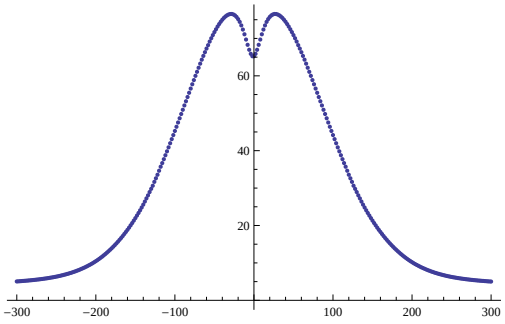

Appendix B

Lithium Density Matrix Calculation

The following is a density matrix calculation for the ^{7}Li D1 line implemented in Mathematica. The author is J. E. Stalnaker. The Atomic Density Matrix (ADM) package found at http://budker.berkeley.edu/ADM/ was used in this calculation. This package was developed by D. Budker and S. Rochester. The ADM package was accessed on Jan. 28, 2013.

Density Matrix Calculation for ^{7}Li D_1 Line

Load Atomic Density Matrix and Other Packages

```
<< AtomicDensityMatrix`

ParallelEvaluate[<< AtomicDensityMatrix`];

Needs["DifferentialEquations`NDSolveProblems`"];
Needs["DifferentialEquations`NDSolveUtilities`"];

<< PlotLegends`
```

Parameters

```
values = {
   α → 3000,
   ω0 → 446 800 129.853, (*Center of Gravity for D1 Transition in MHz*)
   Γ → 6, (*Natrual Linewidth in MHz*)
   ΩR → 10, (*Rabi Frequnecy in MHz*)
   γT → 0.1, (*Transit Linewidth in MHz*)
   k → 1/(671. × 10^-7) 1/10^6, (*k in units of 1/cm*)
   (*e→1,
   ReducedME[1,{Dipole,1},2]→1,*)
   BranchingRatio[2, 1] → 1 (*Branching Ratio for ²P3/2 Decay to ²S1/2*)
  };
```

Define Atomic System

Ground State is labeled "1" and Excited State is labeled "2"

```
sys = Sublevels@{
    AtomicState[1, J → 1/2, L → 0, S → 1/2,
     NuclearSpin → 3/2, Energy → 0, NaturalWidth → 0, HyperfineA → 401.752],
    AtomicState[2, J → 1/2, L → 1, S → 1/2, NuclearSpin → 3/2,
     Energy → ω0, NaturalWidth → Γ, HyperfineA → 45.914]
   };(*Hyperfine Coefficients from Arimondo - ignores the J-J mixing*)
```

Display Density Matrix

```
DensityMatrix[sys] // MatrixForm
```

Define Optical Field

```
optf = OpticalField[ω + k v, E0, {0, 0}] +
  OpticalField[ω - k v, E0, {0, 0}](*x-polarized light*)
```

$$\left\{e^{-i\,t\,(-k\,v+\omega)}\ E0 + e^{-i\,t\,(k\,v+\omega)}\ E0,\ 0,\ 0\right\}$$

Define Hamiltonian

```
(Simplify[h = Hamiltonian[sys,
     ElectricField → (optf /. E0 → ΩR / ReducedME[1, {Dipole, 1}, 2])]]) // MatrixForm
```

Unitary Matrix for Rotating Wave Approximation

```
uRWA = MatrixExp[𝑖 t DiagonalMatrix[Table[If[i ≤ 8, 0, ω], {i, 1, 16}]]];
```

Hamiltonian in the Rotating Frame

Transformed Hamiltonian before RWA

```
(hPrime = hRWA /. {e^(2 𝑖 t (Δ+ω0)) → 0, e^(-2 𝑖 t (Δ+ω0)) → 0}) // MatrixForm // Simplify
```

Relaxation Hamiltonian

```
MatrixForm[relax = IntrinsicRelaxation[sys] + TransitRelaxation[sys, γT]];
```

Repopulation Hamiltonian

```
MatrixForm[repop = OpticalRepopulation[sys] + TransitRepopulation[sys, γT]];
```

Equations of Motion

```
TableForm[eqs = Flatten@LiouvilleEquation[sys, hPrime, relax, repop] //. values]
```

Solutions to Equations of Motion for Different Values of Δ

```
TableForm[inits = Flatten@
    InitialConditions[sys, Table[If[i ≤ 8 && i == j, 1/8, 0], {i, 1, 16}, {j, 1, 16}], 0]];
```

Calculate the spectrum for the zero-velocity class

```
AbsoluteTiming[
 pV0 = Table[DensityMatrix[sys] //. NDSolve[{eqs /. values /. {v → 0}, inits}, DMVariables[
        sys], {t, 0, 1}, AccuracyGoal → 2, PrecisionGoal → 3][[1]], {Δ, -500, 800, 5}];]
```

```
{89.7001576, Null}
```

```
Do[
  {deltaI = ToString[ΔIndex];
   ToExpression["pΔ" <> deltaI][t_] = pV0[[ΔIndex]];},
  {ΔIndex, 1, 1300/5 + 1}];
```

```
AbsoluteTiming[excStatePopV0 = Table[{(deltaI - 1) (5) - 500,
     Sum[Mean[Table[ToExpression["pΔ" <> ToString[deltaI]][t][[j]][[j]], {t, 0, 1, 0.1}]],
      {j, 9, 16}]}, {deltaI, 1, 1300/5 + 1}];]
```

```
{13.0104229, Null}
```

```
ListPlot[excStatePopV0, PlotRange → All, Joined → True]
```

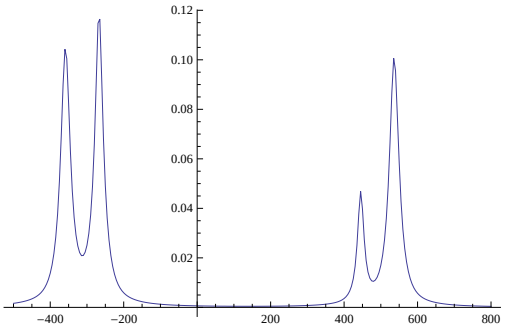

Calculate the spectrum over a range of velocity classes

```
startFreq = −600;
stopFreq = −100;
δf = 2;
startV = 0;
stopV = 7000;
δV = 100;
freqSteps = (stopFreq − startFreq)/δf + 1;
vSteps = (stopV − startV)/δV + 1;
pVel = {};
AbsoluteTiming[
 Do[{
    p = ParallelTable[DensityMatrix[sys] //. NDSolve[{eqs /. values /. v → vi, inits},
          DMVariables[sys], {t, 0, 1.5}, Method → {"StiffnessSwitching"},
          AccuracyGoal → 6, PrecisionGoal → 6][[1]], {Δ, startFreq, stopFreq, δf}];

    Do[
     {deltaI = ToString[ΔIndex];
      ToExpression["pΔ" <> deltaI][t_] = p[[ΔIndex]];},
     {ΔIndex, 1, (stopFreq − startFreq)/δf + 1}];

    excStatePop = Table[{(deltaI − 1) δf + startFreq,
       Mean[Table[ToExpression["pΔ" <> ToString[deltaI]][t], {t, 0, 1.5, 0.1}]]},
      {deltaI, 1, (stopFreq − startFreq)/δf + 1}];

    pVel = Append[pVel, excStatePop];
    If[Mod[vi, 1000] == 0, Print[vi]];
   }, {vi, startV, stopV, δV}];]
```

Doppler Distribution

```
dopDist[v_] := e^(-v^2/a^2) /. values
```

Sum the excited state populations over the velocity class

```
AbsoluteTiming[excStatePopV = Table[{pVel[[1]][[deltaI]][[1]],
    Sum[dopDist[vI δV + startV] pVel[[vI]][[deltaI]][[2]][[j]][[j]], {j, 9, 16},
      {vI, 1, (stopV - startV)/δV + 1}] + Sum[dopDist[vI δV + startV] pVel[[vI]][[deltaI]][[2]][[j]][[j]],
      {j, 9, 16}, {vI, 2, (stopV - startV)/δV + 1}]}, {deltaI, 1, (stopFreq - startFreq)/δf + 1}];]
```

```
{5.5273162, Null}
```

```
ListPlot[{Table[{excStatePopV0[[i]][[1]], 10 excStatePopV0[[i]][[2]]}, {i, 1, 100}],
  excStatePopV}, PlotRange → All, Joined → True]
```

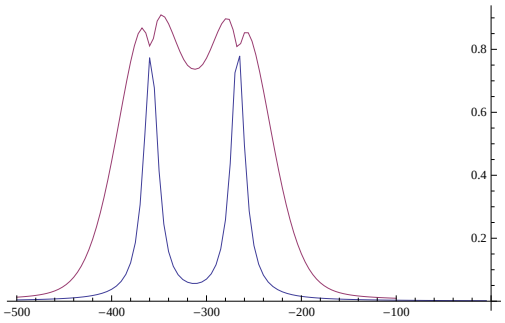

Density Matrix Function formed from the Interplation for the above list

```
ρFn = Interpolation[Table[
   {pVel[[1]][[deltaI]][[1]],
    Sum[dopDist[vI δV + startV] pVel[[vI]][[deltaI]][[2]], {vI, 1, (stopV - startV)/δV + 1}] +
     Sum[dopDist[vI δV + startV] pVel[[vI]][[deltaI]][[2]], {vI, 2, (stopV - startV)/δV + 1}]},
   {deltaI, 1, (stopFreq - startFreq)/δf + 1}]]
```

```
Plot[{ρFn[Δ][[9]][[9]], ρFn[Δ][[10]][[10]], ρFn[Δ][[11]][[11]], ρFn[Δ][[12]][[12]], ρFn[Δ][[13]][[13]],
  ρFn[Δ][[14]][[14]], ρFn[Δ][[15]][[15]], ρFn[Δ][[16]][[16]]}, {Δ, -500, -100}, PlotRange → All]
```

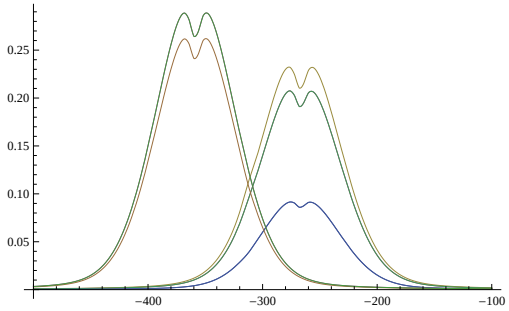

Calculates the Elements of the Fluorescence Matrix for Detection at angle θ relative to z axis.

Excitation is assumed along x - axis. So, $\theta = 0$ means the excitation light is polarized perpendicular to the direction of detection. The fluorescence is broken down into components polarized in the x - z plane and components polarized in the y direction. The sum of the two is used to define the total fluorescence matrix.

This calculates the relative transition strengths for the fluorescence matrix for the decay light polarized in the x - z plane

```
fullWEMatrixFnXZPlane[θ_] =
  (1/√2 (Cos[θ] WignerEckart[sys, {Dipole, 1, -1}]) - 1/√2 (Cos[θ] WignerEckart[
          sys, {Dipole, 1, +1}]) + Sin[θ] WignerEckart[sys, {Dipole, 1, 0}]) .
    Transpose[(1/√2 (Cos[θ] WignerEckart[sys, {Dipole, 1, -1}]) -
       1/√2 (Cos[θ] WignerEckart[sys, {Dipole, 1, +1}]) +
       Sin[θ] WignerEckart[sys, {Dipole, 1, 0}])] /.
   ReducedME[1, {Dipole, 1}, 2] → 1 //. values;
```

This calculates the relative transition strengths for the fluorescence matrix for the decay light polarized in the y direction

```
fullWEMatrixFnY =
  (i/√2 (WignerEckart[sys, {Dipole, 1, -1}] + WignerEckart[sys, {Dipole, 1, +1}])) .
    Transpose[
     (-i/√2 (WignerEckart[sys, {Dipole, 1, -1}] + WignerEckart[sys, {Dipole, 1, +1}]))] /.
   ReducedME[1, {Dipole, 1}, 2] → 1 //. values;
```

Adds the two flurescence matrices, zeroing out the ground-state elements.

```
fluoresOperator[θ_] = Table[If[i > 8 && j > 8,
    fullWEMatrixFnXZPlane[θ][[i]][[j]] + fullWEMatrixFnY[[i]][[j]], 0], {i, 1, 16}, {j, 1, 16}];
```

Fluorescence if only the light polarized in the x-z plane is detected

```
fluoresOperatorXZ[θ_] =
  Table[If[i > 8 && j > 8, fullWEMatrixFnXZPlane[θ][[i]][[j]], 0], {i, 1, 16}, {j, 1, 16}];
```

Fluorescence if only the light polarized in the x-z plane is detected

```
fluoresOperatorY[θ_] =
  Table[If[i > 8 && j > 8, fullWEMatrixFnY[[i]][[j]], 0], {i, 1, 16}, {j, 1, 16}];
```

Fluorescence Function

```
fluoresFn[Δ_, θ_] = Chop[Tr[fluoresOperator[θ].ρFn[Δ] //. values]];
```

```
fluoresYFn[Δ_, θ_] = Chop[Tr[fluoresOperatorY[θ].ρFn[Δ] //. values]];
```

```
fluoresXZFn[Δ_, θ_] = Chop[Tr[fluoresOperatorXZ[θ].ρFn[Δ] //. values]];
```

Results

F=2 to F' Transitions

```
GraphicsGrid[
 {{Plot[{fluoresFn[Δ, 0]}, {Δ, -500, -100}, PlotRange → All, PlotStyle → {Red},
    PlotLegend → "θ=0", LegendShadow → None, LegendPosition → {0.4, 0.25},
    LegendSize → {0.4, 0.25}, LegendBorder → None],
   Plot[{fluoresFn[Δ, 51 π/180]}, {Δ, -500, -100}, PlotRange → All,
    PlotStyle → {Blue}, PlotLegend → "θ=54.7°", LegendShadow → None,
    LegendPosition → {0.4, 0.25}, LegendSize → {0.4, 0.25}, LegendBorder → None],
   Plot[{fluoresFn[Δ, π/2]}, {Δ, -500, -100}, PlotRange → All,
    PlotStyle → {Green}, PlotLegend → "θ=π/2", LegendShadow → None,
    LegendPosition → {0.4, 0.25}, LegendSize → {0.4, 0.25}, LegendBorder → None]}}]
```